10/3-24-97 JSD (1)

X

SANDIA REPORT

SAND97-8241 • UC–401
Unlimited Release
Printed March 1997

Modeling High-Density-Plasma Deposition of SiO_2 in $SiH_4/O_2/Ar$

E. Meeks, R. S. Larson, P. Ho, S. M. Han, E. Edelberg, E. Aydil, and C. Apblett

Prepared by
Sandia National Laboratories
Albuquerque, New Mexico 87185 and Livermore, California 94551
for the United States Department of Energy
under Contract DE-AC04-94AL85000

Approved for public release; distribution is unlimited.

Issued by Sandia National Laboratories, operated for the United States Department of Energy by Sandia Corporation.

Available to DOE and DOE contractors from:

Office of Scientific and Technical Information
P.O. Box 62
Oak Ridge TN 37831

Prices available from (615) 576-8401, FTS 626-8401.

Available to the public from:

National Technical Information Service
U.S. Department of Commerce
5285 Port Royal Rd.
Springfield, VA 22161

UC-401
SAND97-8241
Unlimited Release
Printed March 1997

MODELING HIGH-DENSITY-PLASMA DEPOSITION OF SiO_2 IN $SiH_4/O_2/AR$

Ellen Meeks†, Richard S. Larson†, Pauline Ho‡, and Christopher Apblett‡
Sandia National Laboratories
†Livermore, CA 94551-0969
‡Albuquerque, NM 87185

Sang M. Han, Erik Edelberg, and Eray Aydil
University of California
Santa Barbara, CA 93106-5080

ABSTRACT

We have compiled sets of gas-phase and surface reactions for use in modeling plasma-enhanced chemical vapor deposition of silicon dioxide from silane, oxygen and argon gas mixtures in high-density-plasma reactors. We have applied the reaction mechanisms to modeling three different kinds of high-density plasma deposition chambers, and tested them by comparing model predictions to a variety of experimental measurements. The model simulates a well mixed reactor by solving global conservation equations averaged across the reactor volume. The gas-phase reaction mechanism builds from fundamental electron-impact cross section data available in the literature, and also includes neutral-molecule, ion-ion, and ion-molecule reaction paths. The surface reaction mechanism is based on insight from attenuated total-reflection Fourier-transform infrared spectroscopy experiments. This mechanism describes the adsorption of radical species on an oxide surface, ion-enhanced reactions leading to species desorption from the surface layer, radical abstractions competing for surface sites, and direct energy-dependent ion sputtering of the oxide material. Experimental measurements of total ion densities, relative radical densities as functions of plasma operating conditions, and net deposition-rate have been compared to model predictions to test and modify the chemical kinetics mechanisms. Results show good quantitative agreement between model predictions and experimental measurements.

ACKNOWLEDGMENTS

This work was performed at Sandia National Laboratories as part of a Cooperative Research and Development Agreement with SEMATECH. The authors are grateful to Lam Research Corporation for providing access to experimental data taken at Lam, and to a collaboration with Juan Rey and Junling Li from Technology Modeling Associates on the use of chemistry models in TCAD simulations. This work was supported by the United States Department of Energy under Contract DE-AC04-94AL85000. Sandia is a multiprogram laboratory operated by Sandia Corporation, a Lockheed Martin Company, for the United States Department of Energy.

TABLE OF CONTENTS

Page

LIST OF FIGURES

LIST OF TABLES

Page

I. INTRODUCTION

Deposition of silicon oxide in high-density plasma (HDP) reactors is an important process in constructing multi-level microelectronics devices. In these devices, dielectric layers isolate multiple levels of metal lines, such that the dielectric material properties and film characteristics are critical in determining the device performance and reproducibility. One of the most important characteristics of the silicon oxide films deposited for this application is the ability of the film to reliably fill sub-micron, high-aspect-ratio gaps between metal lines. High density plasma deposition offers unique gap-filling capabilities due to the competition between physical ion sputtering and ion-enhanced chemical vapor deposition processes, which aids in preventing formation of voids within narrow features.[1, 2]

Although much work has been done in investigating the dominant physical processes during gap fill,[1, 3, 2] the relationship between the plasma reactor conditions and how the feature topography evolves during gap fill is not well understood. The motivation for the present work was to provide a physical model of the high density plasma reactor, from which physically based parameters are extracted to simulate topographic evolution during the oxide deposition process. With the goal of improved TCAD (technology computer aided design) simulations, we were also interested in developing a model that is compact in terms of computational resource requirements, while allowing sufficient complexity to capture competing reaction channels over a useful range of reactor operating conditions. The dominant reactions determined from the analyses presented here can later be applied to two or three-dimensional plasma transport simulations in order to gain insight into wafer uniformity issues.

The literature on silane/oxygen kinetics and silane/oxygen plasma chemistry is extensive. However, previous studies have primarily focused on silane combustion occurring at near-atmospheric pressure, or on rf plasmas at medium-pressure (~1 Torr) for oxide deposition. In the case of silane/oxygen plasma modeling, there have been few attempts to make direct comparisons of model predictions of plasma composition with experimental measurements for verifying the set of reaction rate parameters used in the modeling studies. In addition, modeling studies of plasma deposition of silicon oxide have generally used overly simplistic surface reaction mechanisms, limiting the applicability of the models to very restricted process windows. In this work we focus on very low pressure (2-10 mTorr), high charge-density (10^{11} - 10^{12} /cm^3) deposition systems with mixtures of Ar, O_2, and SiH_4 reagent gases. Under these conditions, the surface kinetics play a very important role in determining the plasma composition and behavior, due to high rates of diffusion and low gas-phase reaction rates at the low reactor pressure. We emphasize comparisons with experimental data in representative reactors for ion densities, radical densities, and deposition rates as a means to test our assumptions and to determine an appropriate set of reaction-rate parameters to describe this complex deposition system.

II. REACTOR MODEL

The model employed in the reactor simulations is the Sandia well mixed plasma reactor model, AURORA, described in detail in previous publications.[4, 5] Briefly, the model solves equations resulting from the energy balances of electrons and neutrals, as well as species and mass balances over a specified reactor volume. In addition, the model solves the surface site balances at material surfaces for one or more materials comprising the reactor boundaries. Included in the species balance for each gas-phase species are the net production and loss rates on surfaces weighted by the specified surface area of each material with which the species interacts. The gas energy balance requires a heat transfer coefficient to describe the heat losses from the reactor volume to the external environment. The AURORA model employs the Chemkin-III[6-8] software for describing the kinetics of the gas-phase reactions and the heterogeneous reactions on the various reactor surfaces. The well mixed reactor assumptions require that the plasma composition is determined by chemical kinetics, rather than by transport limitations. This assumption is reasonable for these low pressure (mTorr) reactor simulations, in which species diffusion rates are very fast.[9, 4]

III. GAS-PHASE REACTION MECHANISM

The gas-phase chemical reactions included in our model for the plasma deposition of SiO_2 from SiH_4, O_2, and Ar are given in Table I, including references for the rate constants. In constructing this mechanism, we drew heavily from previous work in the literature. We include 33 gas-phase neutrals, 11 charged species, and two metastables, considering a wide variety of chemical reactions. The electron-impact reactions include electronic and vibrational excitation, ionization, dissociation, and attachment. In general, the electron-impact reaction rate coefficients are determined from fundamental cross-section data and from the assumption of Maxwellian electron energy distribution functions. The reactions among neutral species emphasize atom-transfer and other metathesis reactions, but also account for a number of dissociation and recombination reactions. The model also includes ion-ion neutralization, charge-exchange reactions, and ion-collision-induced atom-transfer reactions where data was available.

In this section we discuss the details of the gas-phase reaction mechanism. In Section V we discuss which reactions are dominant for the HDP conditions. While many of the reactions listed in Table I appear unimportant under these conditions, we have kept them in the mechanism description, both to give the reader an idea of the range of considered reactions and to allow the model to be more predictive with extrapolation capabilities. Under other conditions, the relative importance of the reaction rates may differ.

ELECTRON-IMPACT REACTION KINETICS

In high-plasma-density reactors, the primary gas-phase reactions are electron-impact dissociation and ionization of reagent gases. For argon, oxygen, and silane, the literature provides substantial data on electron collisional processes. We also include electron-impact reactions with O, H, and H_2, because oxygen and silane readily dissociate upon electron impact. To derive the reaction rate parameters given in Table I, we begin with a set of electron-impact cross sections for each molecule, which are given as a function of electron energy for the low-to-medium range of electron energies (threshold to 100s of eV). We have compiled from the literature cross section sets for Ar, O_2, O, SiH_4, H, and H_2, as well as some data on collisions with SiH_x radicals. Assuming a Maxwellian electron energy distribution function (EEDF), the reaction rate coefficient values as a function of mean electron temperature are determined from the integrating

$$k(T_e) = \left(\frac{8}{\pi m_e}\right)^{1/2} \left(\frac{1}{k_B T_e}\right)^{3/2} \int_0^\infty \left\{ \varepsilon \sigma(\varepsilon)\, e^{-\varepsilon/k_B T_e} d\varepsilon \right\}, \qquad (1)$$

where, σ is the electron-energy dependent collision cross section, m_e is the electron mass, k_B is the Boltzmann constant, T_e is the mean electron temperature, and k is the integrated reaction-rate coefficient. The values generated by Eq. (1) are then fit over a range of electron temperature values using the modified Arrhenius form,

$$k(T_e) = AT_e^{\,B} \exp\left(\frac{-C}{T_e}\right). \tag{2}$$

The fitted Arrhenius parameters *A, B,* and *C* are listed in Table I. Although in some cases the functional dependence of the collision cross sections is complex enough to cause difficulties in obtaining good Arrhenius fits to the data generated by Eq. (1). In such cases, we chose the fit parameters such that the match was best (within ~10%) for electron temperatures in the range of 2-6 eV, which should be most relevant to the systems of interest.

The set of electron impact reactions referenced in Table I derive from a number of different sources. Data for oxygen molecules and atoms are primarily from the work of Itikawa, et al.[10, 11] The main deviation from these compilations for oxygen was the use of the dissociation cross section of Cosby[12] in place of the estimate suggested by Itikawa.[10] Data for electron collisions with silane came from the works of Kurachi and Nakamura,[13] Nagpal and Garscadden,[14] and Krishnakumar and Srivastava.[15] For the dissociation of silane, we used the total dissociation rate reported by Kurachi and Nakamura with the branching ratios suggested in previous silane studies[16-18], forming 17% SiH_3 and 83% SiH_2. Data for electron collisions with hydrogen atoms and molecules derived from the extensive compilation of Janev, et al.[19] Finally, recent work by Tarnovsky[20] provided us with cross sections for ionization and dissociative ionization of SiH_x radicals.

While such cross section data are available for the reagent gases and hydrogen, data sets are incomplete for SiH_x ($1<x<4$) fragments, and are unavailable for many of the neutral reaction products. For these secondary species, we include electron-impact reactions with estimated rates when the species densities exceed ~5% of the total density and when measured or calculated cross sections are unavailable. The most important reaction that was estimated in this manner was the electron-impact dissociation of SiH_2O to form SiH and OH. This reaction was included to avoid formation of a significant percentage of a relatively large molecule under plasma conditions that should be highly dissociative. The reaction rate was approximated to be equal to the electron impact dissociation of SiH_4 forming SiH_3 and H. Another relatively large molecule that was treated in a similar manner was Si_2H_2. Here, the electron-impact dissociation rate was estimated from the cross section for electron-impact dissociation of Si_2H_6,[21] while the reaction products were assumed to be two SiH molecules. In a few cases, information was available concerning reaction cross sections, but we chose to omit those reactions in the interest of

simplicity. In particular, we neglected the formation of negative ions from SiH_4, where the cross-sections were small[22] and, when included, resulted in negligible negative-ion densities.

Aside from ionization and dissociation reactions, the electron-impact reaction sets also include a number of vibrational and electronic excitation collisions. In general these are included in order to properly track the electron inelastic energy losses in determining the mean electron temperature. In most cases we do not attempt to track the formation and destruction of different excited states and we assume that rapid quenching on the walls of the reactor return the species to their ground state. The exceptions to that rule are the metastable states, when the contributions of the metastable to ionization or other reaction processes are known to be significant. For this reason we include the Ar^* and O^* metastables as separate species in the chemistry mechanism. The Ar^* ionization cross section is taken from the work of Margreiter, et al.,[23] while the O^* ionization rate is estimated from the ground-state ionization rate, scaling the Arrhenius C parameter (which captures the threshold behavior) by the relative ionization potentials.[9]

NEUTRAL MOLECULE REACTIONS

With 33 neutral molecules included in the model, there are a plethora of possible chemical reactions to consider. Fortunately, many of these reactions have been examined in previous studies of silane CVD, silane pyrolysis and oxidation, or hydrogen combustion.[24-39] We used these previous works in developing the basis for the list of neutral reactions thought to play an important role in plasma deposition of oxide.

As shown in Table I, this approach resulted in a fairly lengthy list of reactions. In some cases, different studies in the literature gave conflicting kinetic parameters for the same reaction. In these cases, we chose to include rate parameters that were directly measured or calculated over those that were inferred or estimated, preferring works that more closely represented the operating conditions in which we were interested for this study. However the uncertainties in the literature illustrates the uncertainties inherent in the rate parameters. In some cases we used this uncertainty as justification for modifying the rate parameters away from the published values in order to give improved agreement between the model and experimental data. These instances are discussed in detail in Section V below and are indicated by footnotes in Table I.

The low total pressures (mTorr) used in these systems put all of the potentially relevant collision-activated unimolecular decomposition and third-body stabilized recombination reactions well into their pressure-dependent regimes. For this reason, such reactions are not included if their rate constants are known only at high pressure (i.e., one atmosphere). The rate constants would be orders of magnitude smaller at the low pressures considered here. Therefore, in the absence of further information, we omitted many recombination reactions

entirely rather than carrying out a full RRKM analysis or including them with a rate constant that was much too high. Nevertheless, the mechanism does include several key third-body reactions whose pressure-falloff behavior has been determined.

ION – MOLECULE REACTIONS

The high density of charged species in HDP reactors requires consideration of ion-neutral and ion-ion collisions. Several compilations of ion chemistry for ions relevant to this study have been reported in the literature.[40-45] While the resulting set of reactions does not include all possible ion-molecule reactions, it does address most interactions between the major ion species (Ar^+, O^+, O_2^+) and the major neutral species (Ar, O, H, H_2, SiH_4). We have found that inclusion of these reactions did not have a very significant effect on simulation results, and so have not pursued estimation of comparable reaction rates for collisions not included in Table I.

THERMOCHEMISTRY OF GAS-PHASE SPECIES

The Chemkin software[6-8] employed in the simulations described in Section III requires that thermochemical data be provided for all species used in the gas-phase and surface reaction mechanisms. These data are used to calculate rate parameters for the back reaction in reversible reactions. In cases where a species only occurs in irreversible reactions, thermochemical data only contributes to the enthalpy gain and loss due to reaction kinetics in the gas and at surfaces for the electron and gas energy balances.

For neutral species, we primarily used two sources of thermochemical data. The Chemkin Thermodynamic Database[7] provided data for H, H_2, O, O_2, O_3, OH, H_2O, HO_2, H_2O_2, Ar and the Si_xH_y (x=1,2) species. For SiO_xH_y species, very little experimental thermochemical information is available in the literature. Therefore, we have used results from quantum chemistry calculations by Allendorf, et al.,[46] and refer the reader to that work for a more detailed discussion of these compounds. For the metastable species Ar^* and O^*, thermochemical data were generated by using the temperature dependent specific heat and entropy data from the ground-state atom and adding the metastable-state excitation energy to the heat of formation of the corresponding atom to determine the enthalpy as a function of temperature.

For charged species, some thermochemical data is available from the JANAF database,[47] specifically for the electron, O^+, O^-, O_2^+, OH^+, H^+, H_2^+, SiH^+, Si^+, and Ar^+ species. For the remaining ions, SiH_2^+ and SiH_3^+, the data were generated by using the temperature dependence of the corresponding neutral species, but replacing the neutral's heat of formation with the ion heat of formation reported in the NIST Structures and Properties Database.[48]

Table I. Gas–phase Mechanism for $SiH_4/O_2/Ar$ Plasma

Rate coefficients in form $k_f = AT^B\exp(-C/T)$.

Units are molecules, centimeters, seconds, and Kelvin.

	Reaction	*A*	*B*	*C*	Notes	Ref.
	(Electron-impact reactions with argon)					
1.	$E + Ar \Rightarrow E + Ar^*$	1.17E-08	0.0	138560.0		49, 50
2.	$E + Ar \Rightarrow Ar^+ + 2E$	7.07E-11	0.6	187120.0		50
3.	$E + Ar^* \Rightarrow Ar^+ + 2E$	1.25E-07	0.1	60524.0		23
	(Electron-impact reactions with oxygen)					
4.	$E + O_2 \Rightarrow O_2 + E$	1.41E-04	-1.5	11594.0	[v], $v_0 \rightarrow v_1$	10
5.	$E + O_2 \Rightarrow O_2 + E$	2.41E-04	-0.9	76827.0	[v], $\Sigma_{n=2,3,4}(v_0 \rightarrow v_n)$	10
6.	$E + O_2 \Rightarrow O_2 + E$	7.13E-08	-0.1	30812.0	[e], a $^1\Delta_g$	10
7.	$E + O_2 \Rightarrow O_2 + E$	2.75E-10	0.0	30656.0	[e], b $^1\Sigma_g^+$	10
8.	$E + O_2 \Rightarrow O_2 + E$	2.29E-10	0.4	68652.0	[e], B $^3\Sigma_u^-$ + A $^3\Sigma_u^+$ + C $^3\Delta_u$ + c $^1\Sigma_u^-$	10
9.	$E + O_2 \Rightarrow O + O^* + E$	4.52E-13	0.9	51069.0		12
10.	$E + O_2 \Rightarrow O_2^+ + 2E$	3.99E-14	1.1	137580.0		10
11.	$E + O_2 \Rightarrow O + O-$	3.60E-08	-0.5	57440.0		10
12.	$E + O \Rightarrow O^* + E$	4.30E-07	-0.3	38431.0	[e], $2p^4\ ^1D$	11
13.	$E + O \Rightarrow O + E$	1.24E-09	0.0	60440.0	[e], $2p^4\ ^1S$	11
14.	$E + O \Rightarrow O + E$	1.67E-09	0.0	146940.0	[e], $3s'\ ^3D^0$	11
15.	$E + O \Rightarrow O + E$	4.36E-09	0.0	110150.0	[e], $3s\ ^3S^0$	11
16.	$E + O \Rightarrow O + E$	1.93E-15	1.1	530780.0	[e], O^{**}	51
17.	$E + O \Rightarrow O^+ + 2E$	1.95E-11	0.6	165410.0		11
18.	$E + O^* \Rightarrow O^+ + 2E$	1.95E-11	0.6	140000.0	[g]	
19.	$E + O^- \Rightarrow O + 2E$	2.10E-10	0.5	39434.0		52
20.	$E + E + O \Rightarrow O^- + E$	1.00E-30	0.0	0.0		11
	(Metastable and ion reactions in O_2/Ar)					
21.	$Ar^* + Ar^* \Rightarrow Ar + Ar^+ + E$	6.20E-10	0.0	0.0		53
22.	$O^- + O_2^+ \Rightarrow O + O_2$	2.80E-07	0.0	0.0	[g]	
23.	$O^- + O^+ \Rightarrow 2O$	2.80E-07	0.0	0.0		40
24.	$O^- + O \Rightarrow O_2 + E$	1.40E-10	0.0	0.0		41
25.	$O^- + Ar^+ \Rightarrow O + Ar$	2.80E-07	0.0	0.0	[g]	
26.	$O^+ + O_2 \Rightarrow O_2^+ + O$	2.10E-11	0.0	0.0		42

[v] This reaction is a vibrational excitation, for which the excited state is indicated in the Notes column, using the notation of the reference providing the cross-section data

[e] This reaction is an electronic excitation, for which the excited state is indicated in the Notes column, using the notation of the reference providing the cross-section data.

[g] The reaction-rate parameters are estimated from those of a similar reaction path.

	Reaction	*A*	*B*	*C*	Notes	Ref.
27.	$O_2^+ + Ar \Rightarrow Ar^+ + O_2$	5.50E-11	0.0	0.0		42
28.	$Ar^+ + O_2 \Rightarrow Ar + O_2^+$	4.60E-11	0.0	0.0		42
29.	$Ar^+ + O \Rightarrow O^+ + Ar$	4.60E-11	0.0	0.0	g	
30.	$O^* + O_2 \Rightarrow O + O_2$	3.20E-11	0.0	-67.0		54
31.	$O^* + O \Rightarrow O + O$	4.00E-11	0.0	0.0		55
32.	$O^* + Ar \Rightarrow Ar + O$	4.00E-11	0.0	0.0	g	
33.	$O + Ar^* \Rightarrow Ar + O$	4.00E-11	0.0	0.0	g	
34.	$O^* + Ar^* \Rightarrow O + Ar$	4.00E-11	0.0	0.0	g	
35.	$O_2 + Ar^* \Rightarrow Ar + O_2$	4.00E-11	0.0	0.0	g	
	(Electron-impact reactions with silane)					
36.	$E + SiH_4 \Rightarrow SiH_4 + E$	1.38E-04	-0.7	43872.0	v, $v_0 \rightarrow v_1$, v_3	13
37.	$E + SiH_4 \Rightarrow SiH_4 + E$	4.52E-03	-1.0	21902.0	v, $v_0 \rightarrow v_2$, v_4	14
38.	$E + SiH_4 \Rightarrow SiH_3 + H + E$	8.96E-03	-1.0	123500.0	d, 17%	13
39.	$E + SiH_4 \Rightarrow SiH_2 + 2H + E$	1.83E-03	-1.0	123500.0	d, 83%	13
40.	$E + SiH_4 \Rightarrow SiH_3^+ + H + 2E$	3.06E-02	-1.3	184820.0		15
41.	$E + SiH_4 \Rightarrow SiH_2^+ + H_2 + 2E$	2.69E-02	-1.2	179670.0		15
42.	$E + SiH_4 \Rightarrow SiH^+ + H_2 + H + 2E$	1.07E-03	-1.2	189440.0		15
43.	$E + SiH_4 \Rightarrow Si^+ + 2H_2 + 2E$	1.58E-03	-1.3	188260.0		15
44.	$E + SiH_4 \Rightarrow H_2^+ + SiH + H + 2E$	1.89E-22	-0.4	22610.0		15
45.	$E + SiH_4 \Rightarrow H^+ + SiH_2 + H + 2E$	9.49E-23	-0.4	20793.0		15
	(Electron-impact reactions with hydrogen)					
46.	$E + H_2 \Rightarrow H_2 + E$	1.40E-05	-0.8	22641.0	v, $v_0 \rightarrow v_1$	19
47.	$E + H_2 \Rightarrow H_2 + E$	4.18E-12	0.6	140680.0	e, B $^1\Sigma_u^+$	19
48.	$E + H_2 \Rightarrow H_2 + E$	6.25E-13	0.8	170230.0	e, C $^1\Pi_u$	19
49.	$E + H_2 \Rightarrow 2H + E$	1.70E-08	0.0	119940.0		19
50.	$E + H_2 \Rightarrow H_2^+ + 2E$	1.33E-13	1.1	197550.0		19
51.	$E + H \Rightarrow H + E$	8.37E-10	0.3	133530.0	e, $1s \rightarrow 2p$	19
52.	$E + H \Rightarrow H^+ + 2E$	7.33E-12	0.7	169360.0		19
	(Other electron-impact processes)					
53.	$E + SiH_3 \Rightarrow SiH_3^+ + 2E$	2.25E-12	0.9	94804.0		20
54.	$E + SiH_3 \Rightarrow SiH_2^+ + H + 2E$	1.70E-11	0.6	133220.0		20
55.	$E + SiH_2 \Rightarrow SiH_2^+ + 2E$	9.16E-12	0.8	98701.0		20
56.	$E + SiH_2 \Rightarrow SiH^+ + H + 2E$	4.39E-11	0.6	146510.0		20
57.	$E + SiH \Rightarrow SiH^+ + 2E$	5.25E-11	0.6	92419.0		20
58.	$E + SiH \Rightarrow Si^+ + H + 2E$	1.33E-12	0.8	125980.0		20
59.	$E + SiH_2O \Rightarrow HSiO + H + E$	8.96E-03	-1.0	123500.0	g	
	(Neutral radical reactions)					
60.	$O + O + M \Leftrightarrow O_2 + M$	5.21E-35	0.0	-900.0		34

[d] This reaction rate is determined assuming the branching ratio indicated under Notes.

	Reaction	*A*	*B*	*C*	Notes	Ref.
61.	$H + SiH_4 \Leftrightarrow H_2 + SiH_3$	2.44E-16	1.9	1102.0		28
62.	$O + SiH_4 \Leftrightarrow OH + SiH_3$	1.23E-10	0.0	1756.0		27
63.	$Si_2 + M \Leftrightarrow Si + Si + M$	1.66E-09	0.0	37460.0		32
64.	$SiH_2 + SiH_2 \Leftrightarrow Si_2H_2 + H_2$	1.08E-09	0.0	0.0		32
65.	$Si + O_2 \Leftrightarrow SiO + O$	2.70E-10	0.0	0.0		30
66.	$H + Si_2H_6 \Leftrightarrow SiH_4 + SiH_3$	1.11E-12	0.0	0.0		56
67.	$H + Si_2H_6 \Leftrightarrow H_2 + Si_2H_5$	2.16E-12	0.0	0.0		56
68.	$SiH_3 + SiH_3 \Leftrightarrow SiH_2 + SiH_4$	2.99E-11	0.0	0.0		57
69.	$SiH_2 + M \Leftrightarrow Si + H_2 + M$	4.98E-09	0.0	19244.0		37
70.	$OH + SiH_4 \Leftrightarrow SiH_3 + H_2O$	1.44E-11	0.0	48.0		25
71.	$SiH_4 + SiH_3 \Leftrightarrow Si_2H_5 + H_2$	2.94E-12	0.0	2214.0		58, 24
72.	$SiH_4 + SiH \Leftrightarrow Si_2H_3 + H_2$	2.41E-12	0.0	1006.0		58, 24
73.	$SiH_2 + H \Leftrightarrow SiH + H_2$	2.31E-11	0.0	0.0	ml	58, 24
74.	$H_2 + Si_2 \Leftrightarrow SiH + SiH$	2.56E-11	0.0	20128.0		58, 24
75.	$H + Si_2 \Leftrightarrow SiH + Si$	8.55E-11	0.0	2667.0		58, 24
76.	$O + O_3 \Leftrightarrow O_2 + O_2$	8.71E-12	0.0	2113.0		31
77.	$O_3 + M \Leftrightarrow O + O_2 + M$	7.17E-10	0.0	11170.0		38
78.	$H_2 + O_2 \Leftrightarrow OH + OH$	2.82E-11	0.0	24043.0		34
79.	$OH + H_2 \Leftrightarrow H_2O + H$	1.94E-15	1.3	1825.0		34
80.	$O + OH \Leftrightarrow O_2 + H$	6.64E-10	-0.5	0.0		34
81.	$O + H_2 \Leftrightarrow OH + H$	8.40E-20	2.7	3165.0		34
82.	$OH + HO_2 \Leftrightarrow H_2O + O_2$	1.24E-11	0.0	0.0		34
83.	$H + HO_2 \Leftrightarrow OH + OH$	2.32E-10	0.0	540.0		34
84.	$O + HO_2 \Leftrightarrow O_2 + OH$	2.33E-11	0.0	540.0		34
85.	$OH + OH \Leftrightarrow O + H_2O$	9.96E-16	1.3	0.0		34
86.	$H + HO_2 \Leftrightarrow H_2 + O_2$	2.08E-11	0.0	0.0		34
87.	$HO_2 + HO_2 \Leftrightarrow H_2O_2 + O_2$	3.32E-12	0.0	0.0		34
88.	$H_2O_2 + M \Leftrightarrow OH + OH + M$	2.16E-07	0.0	22896.0		34
89.	$H_2O_2 + H \Leftrightarrow HO_2 + H_2$	2.66E-12	0.0	1912.0		34
90.	$H_2O_2 + OH \Leftrightarrow H_2O + HO_2$	1.66E-11	0.0	906.0		34
91.	$H + O_2 + M \Leftrightarrow HO_2 + M$	9.95E-31	-0.7	0.0		34
	Enhanced third–body efficiencies: H_2O=18.6, H_2= 2.9					
92.	$H + H + M \Leftrightarrow H_2 + M$	2.76E-30	-1.0	0.0		34
	Enhanced third–body efficiencies: H_2O=0.0, H_2= 0.0					
93.	$H + H + H_2 \Leftrightarrow H_2 + H_2$	2.54E-31	-0.6	0.0		34
94.	$H + H + H_2O \Leftrightarrow H_2 + H_2O$	1.65E-28	-1.2	0.0		34
95.	$H + OH + M \Leftrightarrow H_2O + M$	4.41E-26	-2.0	0.0		34
	Enhanced third–body efficiencies: H_2O = 5.0					

[ml] The activation energy was removed from the referenced estimation of the rate parameters.

	Reaction	*A*	*B*	*C*	Notes	Ref.
96.	$H + O + M \Leftrightarrow OH + M$	1.71E-31	-0.6	0.0		34
	Enhanced third–body efficiencies: $H_2O = 5.0$					
97.	$Si + SiH_2 \Leftrightarrow Si_2 + H_2$	2.49E-10	0.0	0.0		33
98.	$Si + SiH_4 \Leftrightarrow Si_2H_2 + H_2$	2.49E-10	0.0	3669.0		33
99.	$SiH_3(+M) \Leftrightarrow SiH + H_2(+M)$					33
	High–pressure limit:	4.47E+14	-0.6	22492.0		
	Low pressure limit:	3.28E+02	-0.31	22528.0		
100.	$SiH + SiH_4 \Leftrightarrow H_3SiSiH + H$	4.98E-10	0.0	4535.0		33
101.	$SiH_4(+M) \Leftrightarrow SiH_2 + H_2(+M)$					29
	High–pressure limit:	3.12E+09	1.7	27530.0		
	Low pressure limit:	8.65E+05	-0.35	28959.0		
	Troe parameters: $a = -0.49840$, $T^{***} = 888.30$, $T^{*} = 209.40$, $T^{**} = 2760.0$				f	
	Enhanced third–body efficiencies: $SiH_4 = 4.0$, $Si_2H_6 = 4.0$					
102.	$Si_2H_6(+M) \Leftrightarrow SiH_4 + SiH_2(+M)$					29
	High–pressure limit:	1.81E+10	1.7	25262.0		
	Low pressure limit:	8.45E+29	-0.10	28197.0		
	Troe parameters: $a = 0.43750E-04$, $T^{***} = 438.50$, $T^{*} = 2726.0$, $T^{**} = 438.20$				f	
	Enhanced third–body efficiencies: $SiH_4 = 4.0$, $Si_2H_6 = 4.0$					
103.	$Si_2H_6(+M) \Leftrightarrow H_2 + H_3SiSiH(+M)$					29
	High–pressure limit:	9.09E+09	1.8	27272.0		
	Low pressure limit:	3.22E+20	-0.78	29701.0		
	Troe parameters: $a = -0.12240$, $T^{***} = 793.30$, $T^{*} = 2400.0$, $T^{**} = 113.90$				f	
	Enhanced third–body efficiencies: $SiH_4 = 4.0$, $Si_2H_6 = 4.0$					
104.	$H_3SiSiH(+M) \Leftrightarrow H_2SiSiH_2(+M)$					29
	High–pressure limit:	2.54E+13	-0.2	2708.0		
	Low pressure limit:	1.83E+09	-0.58	4605.0		
	Troe parameters: $a = -0.42020E+00$, $T^{***} = 214.50$, $T^{*} = 103.00$, $T^{**} = 136.30$				f	
	Enhanced third–body efficiencies: $SiH_4 = 4.0$, $Si_2H_6 = 4.0$					
105.	$H_3SiSiH + H_2 \Leftrightarrow SiH_2 + SiH_4$	1.56E-10	0.0	2059.0		29
	Reverse Arrhenius coefficients:	1.57E-13	1.1	2914.0		
106.	$H_3SiSiH + SiH_4 \Leftrightarrow Si_2H_6 + SiH_2$	2.87E-10	0.4	4478.0		29
	Reverse Arrhenius coefficients:	4.40E-09	0.1	4264.0		
107.	$H_3SiSiH(+M) \Leftrightarrow Si + SiH_4(+M)$					29
	High–pressure limit:	1.42E+13	0.5	28958.0		
	Low pressure limit:	3.90E+18	-0.74	30674.0		
	Troe parameters: $a = 0.53360E+00$, $T^{***} = 629.20$, $T^{*} = 2190.0$, $T^{**} = 636.50$				f	
	Enhanced third–body efficiencies: $SiH_4 = 4.0$, $Si_2H_6 = 4.0$					

[f] This is a pressure fall-off reaction in the Troe form as described in Reference [59]:

$F_{cent}(T) = (1 - a)\exp(-T/T^{***}) + a\exp(-T/T^{*}) + \exp(-T^{**}/T)$.

	Reaction	*A*	*B*	*C*	Notes	Ref.
108.	$Si + Si_2H_6 \Leftrightarrow SiH_2 + H_3SiSiH$	2.16E-09	0.0	6340.0		29
109.	$SiH_4 + O_2 \Leftrightarrow SiH_3 + HO_2$	3.32E-13	0.0	22141.0		36
110.	$SiH_4 + HO_2 \Leftrightarrow SiH_3 + H_2O_2$	4.98E-12	0.0	2818.0		36
111.	$SiH_3 + H \Leftrightarrow SiH_2 + H_2$	2.49E-11	0.0	1258.0		36
112.	$SiH_3 + O \Leftrightarrow SiH_2O + H$	1.08E-09	0.0	1006.0	m2	36
113.	$SiH_3 + OH \Leftrightarrow SiH_2O + H_2$	8.30E-12	0.0	0.0		36
114.	$SiH_2 + O_2 \Leftrightarrow HSiO + OH$	1.66E-10	0.0	1862.0		36
115.	$SiH_2O + M \Leftrightarrow HSiO + H + M$	8.30E-08	0.0	38546.0		36
116.	$SiH_2O + H \Leftrightarrow HSiO + H_2$	5.48E-10	0.0	5284.0		36
117.	$SiH_2O + O \Leftrightarrow HSiO + OH$	2.99E-11	0.0	1550.0		36
118.	$SiH_2O + OH \Leftrightarrow HSiO + H_2O$	1.24E-11	0.0	86.0		36
119.	$SiH_2O + HO_2 \Leftrightarrow HSiO + H_2O_2$	1.66E-12	0.0	4026.0		36
120.	$HSiO + M \Leftrightarrow SiO + H + M$	8.30E-10	0.0	14593.0		36
121.	$HSiO + H \Leftrightarrow SiO + H_2$	3.32E-10	0.0	0.0		36
122.	$HSiO + O \Leftrightarrow SiO + OH$	8.30E-10	0.0	0.0	m2	36
123.	$HSiO + OH \Leftrightarrow SiO + H_2O$	1.66E-10	0.0	0.0		36
124.	$HSiO + O_2 \Leftrightarrow SiO + HO_2$	1.99E-10	0.0	2000.0		36
125.	$SiO + OH \Leftrightarrow SiO_2 + H$	6.64E-12	0.0	2868.0		36
126.	$SiO + O + M \Leftrightarrow SiO_2 + M$	6.89E-33	0.0	2199.0		36
127.	$SiO + O_2 \Leftrightarrow SiO_2 + O$	1.66E-11	0.0	3271.0		36
128.	$SiH_3 + O_2 \Leftrightarrow SiH_2O + OH$	6.02E-12	0.0	0.0	m3	39
129.	$SiH_3 + O_2 \Leftrightarrow SiH_3O + O$	2.02E-12	0.0	0.0		39
130.	$SiH_3 + O_2 \Leftrightarrow HSiOOH + H$	3.56E-12	0.0	0.0	m4	39
131.	$HO_2 + M \Leftrightarrow O + OH + M$	1.36E-02	-1.0	33161.0		26
132.	$SiH_4 + SiH_3O \Leftrightarrow SiH_3 + SiH_3OH$	3.32E-13	0.0	2667.0		26
133.	$SiH_4 + SiH_3O_2 \Leftrightarrow SiH_3 + SiH_3O_2H$	1.83E-11	0.0	9309.0		26
134.	$SiH_3O_2 + SiH_2O \Leftrightarrow SiH_3O_2H + HSiO$	2.16E-13	0.0	3422.0		26
135.	$SiH_3O_2 + HO_2 \Leftrightarrow SiH_3O_2H + O_2$	6.64E-14	0.0	0.0		26
136.	$SiH_3O_2H + H \Leftrightarrow SiH_3O_2 + H_2$	7.97E-11	0.0	4000.0		26
137.	$SiH_3O + SiH_2O \Leftrightarrow SiH_3OH + HSiO$	1.99E-13	0.0	489.0		26
138.	$SiH_3O + SiH_3OH \Leftrightarrow SiH_3OH + SiH_2OH$	2.49E-12	0.0	2667.0		26
139.	$SiH_3O + O_2 \Leftrightarrow SiH_2O + HO_2$	1.66E-12	0.0	2264.0		26
140.	$SiH_3OH + H \Leftrightarrow SiH_2OH + H_2$	4.98E-11	0.0	2667.0		26
141.	$SiH_3OH + O \Leftrightarrow SiH_2OH + OH$	2.82E-12	0.0	871.0		26
142.	$SiH_3OH + OH \Leftrightarrow SiH_2OH + H_2O$	6.64E-12	0.0	755.0		26
143.	$SiH_3OH + SiH_3 \Leftrightarrow SiH_2OH + SiH_4$	2.99E-13	0.0	3724.0		26

m2 The pre-exponential rate parameter was increased to five times the value referenced.

m3 The pre-exponential rate parameter was increased to two times the value referenced.

m4 The pre-exponential rate parameter was decreased to one half the value referenced.

	Reaction	*A*	*B*	*C*	Notes	Ref.
144.	$SiH_3OH + SiH_3O_2 \Leftrightarrow SiH_2OH + SiH_3O_2H$	1.05E-11	0.0	7296.0		26
145.	$SiH_3OH + O_2 \Leftrightarrow SiH_2OH + HO_2$	6.64E-11	0.0	22644.0		26
146.	$SiH_3OH + HO_2 \Leftrightarrow SiH_2OH + H_2O_2$	1.05E-11	0.0	7045.0		26
147.	$SiH_2O + O_2 \Leftrightarrow HSiO + HO_2$	6.64E-10	0.0	14845.0		26
148.	$SiH_2OH + O_2 \Leftrightarrow HSiOOH + OH$	1.66E-11	0.0	3522.0		26
149.	$HSiO + SiH_3O \Leftrightarrow SiO + SiH_3OH$	1.66E-12	0.0	0.0		26
150.	$SiH_2O + H_2O \Leftrightarrow HSiOOH + H_2$	1.66E-11	0.0	0.0		26
151.	$SiH_2O + OH \Leftrightarrow HSiOOH + H$	1.66E-11	0.0	0.0		26
152.	$SiH_2O + HO_2 \Leftrightarrow HSiOOH + OH$	1.66E-13	0.0	0.0		26
153.	$HSiOOH + O_2 \Leftrightarrow SiOOH + HO_2$	2.82E-11	0.0	8051.0		26
154.	$SiOOH + O_2 \Leftrightarrow SiO_2 + HO_2$	1.66E-12	0.0	7196.0		26
155.	$SiOOH + H \Leftrightarrow SiO_2 + H_2$	1.66E-12	0.0	4529.0		26
156.	$O_2 + SiH \Leftrightarrow SiO + OH$	1.70E-10	0.0	0.0		35
	(Ion-neutral reactions)					
157.	$O^+ + SiH_4 \Rightarrow SiH_3^+ + O + H$	3.20E-11	0.0	0.0		43
158.	$O_2^+ + SiH_4 \Rightarrow SiH_3^+ + H + O_2$	2.00E-10	0.0	0.0		43
159.	$O_2^+ + SiH_4 \Rightarrow SiH_2^+ + H_2 + O_2$	1.00E-10	0.0	0.0		43
160.	$H_2^+ + Ar \Rightarrow Ar^+ + H_2$	3.00E-10	0.0	0.0		44
161.	$Ar^+ + H_2 \Rightarrow H_2^+ + Ar$	1.30E-10	0.0	0.0		44
162.	$H^+ + SiH_4 \Rightarrow SiH_3^+ + H_2$	5.00E-09	0.0	0.0		45
163.	$H_2^+ + SiH_4 \Rightarrow SiH_3^+ + H_2 + H$	3.60E-09	0.0	0.0		45
164.	$SiH_2^+ + SiH_4 \Rightarrow SiH_3^+ + SiH_3$	1.10E-09	0.0	0.0		45
165.	$Ar^+ + SiH_4 \Rightarrow Ar + SiH_3^+ + H$	1.70E-11	0.0	0.0		45
166.	$Ar^+ + SiH_4 \Rightarrow Ar + SiH_2^+ + H_2$	3.90E-11	0.0	0.0		45
167.	$Ar^+ + SiH_4 \Rightarrow Ar + SiH^+ + H + H_2$	8.00E-11	0.0	0.0		45

III. SURFACE DEPOSITION CHEMISTRY

The development of a reaction mechanism for the surface chemistry is much less straightforward than the gas-phase chemistry. To facilitate this task, we adopt the formalism of the Surface Chemkin{Coltrin, 1996 #163} software to describe the surface kinetics. This formalism defines a surface species to be the chemical species on the top-most layer of the solid, at the interface between the solid and the gas. Each surface species occupies one or more "sites" and, in this work, the total number of surface sites is conserved. Below the surface layer, we define "bulk" species that may be created or destroyed due to deposition or etch processes. Using this approach, it is possible to construct a self-consistent and physically realistic set of reactions by suitably modifying the scheme proposed by Moffat[60] for the deposition of SiO_2 from tetraethylorthosilicate (TEOS). In the present case, this involves defining a total of 13 different surface species, each of which is centered on a single silicon atom. Such an atom can share at most four bonds with either H, OH, or "G"; the latter stands for "glass" and is simply defined as an oxygen atom that is shared with another Si. A surface species can be either saturated with various combinations of OH, H, or G bonds or unsaturated with one or more dangling bonds; examples are $SiG(OH)H_2$ and SiG(OH)H, respectively. Furthermore, the bulk species, SiO_2, deposited by a series of reaction steps described below, is exactly equivalent to SiG_4. With this formalism in place, we are able to postulate reaction paths by which the surface species are formed and are ultimately converted to bulk SiO_2.

The surface reactions used in our model are listed in Table II, along with the rate coefficients or reaction-probability parameters. Although the list of surface reactions of neutral species in Table II is long, it actually consists of only a few classes of reactions. Most of the reactions represent the reaction of a gas-phase species with a surface species where the reaction rate is expressed in the form of a "sticking coefficient" or "reaction probability". In the case of ion reactions with the surface, a similar reaction probability formulation is used, although the limiting ion flux is assumed to be the Bohm flux (proportional to the square root of the electron energy) rather than the thermal flux used for the neutral species. In many cases we express the reaction probability for an ion-surface interaction in the form of an ion-energy-dependent yield function. In this way, for the same ion flux to the surface, the rate of ion-induced reaction events can vary depending on the ion energy.

In the plasma deposition system, ions bombard the substrate surface with fluxes comparable in magnitude to the neutral species fluxes. There has been much recent speculation as to the role of these ions in forming the deposited film. For the systems in which we are interested, the reagent gases are diluted by 30% or greater with argon, such that the dominant ion hitting the surface is Ar^+. Unless there are significant charge-exchange reactions not accounted for in our mechanism, our model suggests that the silicon-containing ion fluxes are not sufficient

to account directly for more than about 20% of the deposition rates observed in these systems. However, we have included the possibility of such direct deposition from ions in our surface mechanism. In addition, we assume that the ion bombardment of the surface plays two key roles in the deposition process: 1) it enhances adsorption and desorption rates of neutral radical species through bond-breaking and roughening of the top monolayers of the film, and 2) it directly sputters deposited SiO_2 from the surface. The details of this approach are described further below.

REACTIONS OF NEUTRALS ON SURFACE SITES

The first set of reactions in the mechanism, shown in Table II, accounts for deposition of bulk SiO_2 from gas-phase silicon-containing radicals reacting with the surface species $SiG_3(OH)$. Recent *in situ* studies using attenuated total reflection Fourier-transform infrared spectroscopy (ATR-FTIR) showed that reactions of silane fragments with surface hydroxyls can be one of the steps that lead to deposition.[61] In our model, each step involving the addition of a silicon-containing species produces bulk SiO_2, as well as a new but different surface species to propagate the chain and conserve surface sites. The ATR-FTIR experiments by Han and Aydil[61] also showed that thermal decomposition of SiH_4 in the absence of the plasma is an insignificant channel for incorporating Si onto the surface. We therefore neglect reactions of saturated gas-phase species such as SiH_4 with the surface. For surface species other than $SiG_3(OH)$, we considered non-deposition reactions to be the most likely to occur; among these reactions are intramolecular elimination of H_2 or H_2O or (for unsaturated species) attachment of other gas-phase radicals. Finally, direct deposition of gas-phase SiO_2 is included in the mechanism for completeness, although the contribution to total deposition rate is negligible. In view of the limited information available, we have not included all possible combinations of surface ligands although the nomenclature system and software are flexible enough to do so. We have also not differentiated between isolated and paired Si-OH groups, although such groups are known,[61] but rather treat them as equivalent species. All deposition reactions involving deposition of bulk SiO_2 are written as irreversible, because SiO_2 does not decompose at typical deposition temperatures (200-450°C).

The remaining reactions in the mechanism account for various methods of conversion between the surface species. The intramolecular eliminations of H_2 and H_2O form glass bonds between the Si and O as well as reducing the amount of hydrogen on the surface. For simplicity, only intramolecular eliminations are included although intermolecular eliminations probably also occur. The other surface reactions involve the attack of a surface species by a gas-phase radical or molecule. If the surface species in question is unsaturated, then either an H or an OH radical can attach to the dangling bond. If the surface species has at least two dangling bonds, then dissociative attachment of either H_2, H_2O, or H_2O_2 is possible. The most likely reaction for

oxygen atoms is the oxidation of surface hydrogens, i.e., the conversion of H to OH. Finally, the radicals H and OH can attack saturated surface species by abstracting H to form gas-phase H_2 and H_2O, respectively. Although this unsaturates the surface, it also leads to a more stable gaseous species. Clearly, many other surface reactions could be postulated, but those listed here are considered to be the most likely, based upon the observations of *in situ* ATR-FTIR experiments.

The assignment of rate constants to the surface reactions is largely a matter of educated guesswork. However, for all of the reactions involving gas-phase species, the level of uncertainty is reduced by assigning values to a reactive sticking coefficient rather than separately estimating activation energies and pre-exponential factors. Independent knowledge of the activation energy for a given process is used where available, even if the magnitude of the sticking coefficient must be estimated. In many cases, we obtained information on activation energies from analogous gas-phase reactions. Ultimately, the sticking coefficients are adjusted within reasonable limits to achieve a satisfactory fit of the experimental data.

ION-INDUCED CHEMICAL REACTIONS

Previous experimental work by Han and Aydil[61] examined surface bonding structure during oxide film growth, both with and without ion bombardment. Their results showed a conversion of associated OH species that are weakly bound on the surface, to isolated Si-OH bonds through the desorption of H_2O when ion bombardment was present. Following these observations, our mechanism includes ion-induced elimination of H_2O, which forms $SiG_3(OH)$ from other surface species and allows deposition to proceed. A thermal path for the surface-species conversion is also included, but the thermal rate is set low, such that the ion-enhanced elimination dominates. Reactions similar to the ion-induced H_2O desorption are also included for ion-enhanced H_2 desorption from hydrogenated surface species.

Although the model predictions of each individual ion flux to the surface will depend on the ion mass (to the $-1/2$ power) and directly on the ion density, the ions are otherwise treated equivalently in their contribution to the ion-enhanced deposition reactions. For each ion, the total ion flux is limited by the Bohm criterion, such that

$$\Gamma_i = \xi n_i \left(\frac{k_B T_e}{m_i} \right)^{1/2} . \tag{3}$$

In Eq. 3, Γ_i is the flux of the ith ion, n_i is the ion density, m_i is the ion mass, and ξ represents the ratio of the ion density at the sheath edge to the ion density in the bulk of the plasma. The value used for ξ in for our reactor simulations is between 0.6 and 0.7, as suggested by Lieberman and

Lichtenberg.[62] While the ion flux is limited in this way, there several different reaction paths may result from the ion bombardment. We therefore define a reaction probability analogous to a sticking coefficient, such that the rate of progress for a specific reaction will be $q_r = \gamma\Gamma_i$, where γ is the reaction probability. In addition to this formulation, we also allow for the rate of production of reaction product to depend on an ion-energy-dependent yield function. For example, the reaction,

$$Ar^+ + e + ySiG(OH)_3 \Rightarrow Ar + ySiG_3(OH) + yH_2O \tag{4}$$

is written such that the rate of production of H_2O and the rate of destruction of $SiG(OH)_3$ are equal to yq_r, while the rate of ion neutralization is just q_r. The yield parameter y is defined by:

$$\begin{aligned} y &= A\left(E_i^a - E_{th}^a\right)^b, && E_i > E_{th} \\ y &= 0.0, && E_i \le E_{th}. \end{aligned} \tag{5}$$

In Eq. 5, E_{th} is the threshold energy and E_i is the energy of the ions hitting the surface after they have been accelerated by the plasma sheath. The parameters A, E_{th}, a, and b for the relevant reactions are given in Table II, but in all the reactions listed a=0.5 and b=0.0, such that the yield depends directly on the ion momentum. In our model, the ion energy for each set of conditions is estimated from the substrate rf-bias power, the ion current calculated in the model, and any measured voltage data available for the reactor system. The values used vary from 15-150eV and are discussed further in the Section V.

PHYSICAL SPUTTERING BY IONS

In addition to ion-enhanced deposition, high-energy ion bombardment can lead to direct sputtering of deposited material from the wafer surface. This process in fact plays a critical role in determining the gap-filling characteristics of the deposited films. In addition to ion-energy dependence, the ion sputtering depends strongly on the angle of incidence of the incoming ion. The ion-angular dependence causes facets to form at the opening of a gap in which the film is deposited, preventing the deposition process from producing unwanted voids within the gaps. In the work reported here, we are primarily interested in testing the blanket deposition behavior of our model, and therefore only consider ion bombardment normal to the deposition surface. However, direct ion sputtering significantly lowers the net deposition rates and must be included in the model. The ion yield parameters (see Eq. (5)) used for the sputtering reactions are listed in Table II. In all cases, the parameters a and b are set to 0.5 and 0.0, respectively, while the yield threshold, E_{th} is estimated to be 35eV based on deposition-rate and bias-voltage measurements made at Lam Research Corporation.[63] With these parameters set, we then determined the yield magnitude by matching the yield values at high energies to the experimental data reported by

Scaglione, et al[64]. Scaglione provided data for both argon and nitrogen ion sputtering of silicon dioxide.[64] We used the argon data directly and used the nitrogen ion data as an estimate for oxygen ion sputtering. Molecular oxygen ions were assumed to dissociate upon impact, such that they have twice the yield as atomic ions at one-half of the energy. All other ion yields were estimated based on the mass of the ion. The resulting ion yield functions are shown in Figure 1.

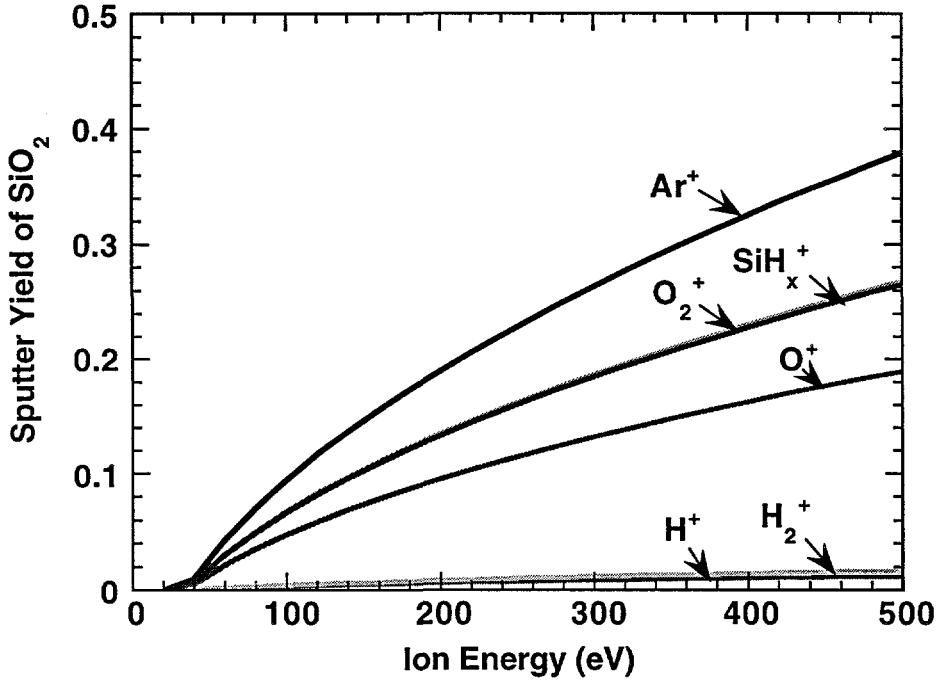

Figure 1. The ion yield functions used in the simulations for physical sputtering of bulk SiO_2. The yield functions are represented in Table I by fitting coefficients from Eq. (5).

WALL RECOMBINATION REACTIONS

In addition to heterogeneous reactions occurring on the wafer surface in a wafer-processing reactor, reactions can also occur on the walls of the reactor chamber. Most importantly for the plasma model, we must include ion recombination losses at the reactor walls. These reactions serve as the primary loss mechanism for the ions in the plasma, balance the electron-impact production rates, and are critical to determining the mean electron temperature. Also, we assume that collisions with the chamber walls provide quenching of the metastable species with 100% efficiency. Finally, some oxide deposition is likely to occur on the reactor walls (up to 10-20% of that on the wafer[63]), which provides a loss mechanism for the neutral radical species. Rather than including a separate wall-deposition mechanism, these parasitic deposition processes are included by effectively increasing the area of the deposition surface by 10% of the reactor wall area.

THERMOCHEMISTRY OF SURFACE SPECIES

For the bulk species $SiO_2(D)$, we obtained thermochemical data from Babushkin et al.[65] Thermochemical data for surface species, however, are rarely available in the literature. We have therefore estimated the necessary data by semi-empirical methods, using as a starting point the values given by Moffat[60] for similar species in the TEOS system. In the work by Moffat, thermochemical data were obtained by extending standard estimation methods for gas-phase compounds to surface species. Specifically, heats of formation were estimated using the group contribution approach developed by Benson,[66] based primarily on group values published by Walsh[67] for silicon-containing compounds. Entropies and heat capacities were determined by estimating necessary vibrational frequencies and applying statistical mechanical formulas. In the present work, we use directly the properties computed by Moffat for $SiG_3(OH)$. However, rather than attempting to perform similar calculations for the remaining surface species in our mechanism, we have opted for a simpler, less fundamental approach based on analogies. This is deemed appropriate in view of the uncertainties in the molecular parameters. The estimation methods used to determine enthalpies, entropies, and heat capacities differ from each other, and so are described separately below.

Starting with enthalpies, a value for $SiG(OH)_3$ (at a base temperature of 573 K) was first computed from the values for similar species in the TEOS system by assuming that the effect of replacing an ethoxy group (E) with a hydroxyl group (OH) is independent of the nature of the other substituents. Thus,

$$H^\circ\left(\mathrm{SiG(OH)_3}\right) - H^\circ\left(\mathrm{SiG(OH)_2E}\right) = H^\circ\left(\mathrm{SiG(OH)_2E}\right) - H^\circ\left(\mathrm{SiG(OH)E_2}\right)$$

Enthalpies for the remaining surface species were then calculated sequentially by assuming that the effect of changing or deleting a substituent was the same as in the gas phase, with the glass bond (G) being replaced by OH. For example,

$$H^\circ\left(\mathrm{SiG(OH)_2H}\right) - H^\circ\left(\mathrm{SiG(OH)_3}\right) = H^\circ\left(\mathrm{Si(OH)_3H}\right) - H^\circ\left(\mathrm{Si(OH)_4}\right)$$
$$H^\circ\left(\mathrm{SiG(OH)_2}\right) - H^\circ\left(\mathrm{SiG(OH)_3}\right) = H^\circ\left(\mathrm{Si(OH)_3}\right) - H^\circ\left(\mathrm{Si(OH)_4}\right)$$

This approach is inappropriate for calculating entropies (partly because of symmetry issues), so values of S at 573 K were estimated by a group contribution method instead. First, a least-squares fitting procedure was applied to entropy values for surface species in the TEOS system to extract group contributions for Si, G, and OH (as well as E). In the absence of any other data, a group contribution for H was found by applying a similar fitting procedure to entropy data for gas-phase silanes, silanols, and related radicals. The desired entropies were then

calculated by simply adding up the group contributions in the correct proportions.

The same procedure was used to estimate heat capacities for the surface species, except that calculations were carried out at various temperatures ranging from 300 K to 1000 K. The results for each species were then fit with a quartic (fourth-degree) polynomial in T. The heat capacity coefficients calculated in this way were combined with the previously obtained enthalpy and entropy to produce a thermodynamic data base entry in the standard Chemkin[7, 8] format.

Table II. Surface Mechanism for SiO_2 Deposition from $SiH_4/O_2/Ar$ Plasma

Reaction rate coefficients are in the form $k_f = A \exp(-C/T)$.

Sticking coefficients are in form $\gamma = A \exp(-C/T)$.

Yield coefficients are in the form $y = a\,(E_i^b - E_{th}^b)^c$

Units are molecules, centimeters, seconds, and Kelvin.

	Reaction	A	C	Notes
	(Deposition of silicon-containing radicals)			
1.	$SiH_3 + SiG_3(OH) \Rightarrow SiGH_2 + SiO_2(D) + H_2$	1.0	0.0	s
2.	$SiH_2 + SiG_3(OH) \Rightarrow SiGH + SiO_2(D) + H_2$	1.0	0.0	s
3.	$SiH + SiG_3(OH) \Rightarrow SiG + SiO_2(D) + H_2$	1.0	0.0	s
4.	$Si + SiG_3(OH) \Rightarrow SiGH + SiO_2(D)$	1.0	0.0	s
5.	$SiO + SiG_3(OH) \Rightarrow SiG(OH) + SiO_2(D)$	1.0	0.0	s
6.	$HSiO + SiG_3(OH) \Rightarrow SiG(OH)H + SiO_2(D)$	1.0	0.0	s
7.	$SiH_3O + SiG_3(OH) \Rightarrow SiGH_3 + SiO_2(D) + OH$	1.0	0.0	s
	(Direct deposition of SiO_2)			
8.	$SiO_2 \Rightarrow SiO_2(D)$	1.0	0.0	s
	(Intramolecular elimination of H_2 and H_2O - thermal path)			
9.	$SiG(OH)_2H \Leftrightarrow SiG_3(OH) + H_2$	2.00E+10	15000.0	
10.	$SiG(OH)H_2 \Leftrightarrow SiG_3H + H_2$	2.00E+10	15000.0	
11.	$SiG(OH)H \Leftrightarrow SiG_3 + H_2$	2.00E+10	15000.0	
12.	$SiG(OH)_3 \Leftrightarrow SiG_3(OH) + H_2O$	2.00E+10	15000.0	
13.	$SiG(OH)_2H \Leftrightarrow SiG_3H + H_2O$	2.00E+10	15000.0	
14.	$SiG(OH)_2 \Leftrightarrow SiG_3 + H_2O$	2.00E+10	15000.0	
	(Oxidation of surface hydrogens)			
15.	$SiG_3H + O \Leftrightarrow SiG_3(OH)$	0.4	0.0	s
16.	$SiG(OH)_2H + O \Leftrightarrow SiG(OH)_3$	0.4	0.0	s
17.	$SiG(OH)H_2 + O \Leftrightarrow SiG(OH)_2H$	0.4	0.0	s
18.	$SiGH_3 + O \Leftrightarrow SiG(OH)H_2$	0.4	0.0	s
19.	$SiG(OH)H + O \Leftrightarrow SiG(OH)_2$	0.4	0.0	s
20.	$SiGH_2 + O \Leftrightarrow SiG(OH)H$	0.4	0.0	s
21.	$SiGH + O \Leftrightarrow SiG(OH)$	0.4	0.0	s

[s] The reaction-rate parameters are for reactive sticking coefficients.

	Reaction	*A*	*C*	Notes
22.	$SiG_3H + O^* \Leftrightarrow SiG_3(OH)$	0.4	0.0	s
23.	$SiG(OH)_2H + O^* \Leftrightarrow SiG(OH)_3$	0.4	0.0	s
24.	$SiG(OH)H_2 + O^* \Leftrightarrow SiG(OH)_2H$	0.4	0.0	s
25.	$SiGH_3 + O^* \Leftrightarrow SiG(OH)H_2$	0.4	0.0	s
26.	$SiG(OH)H + O^* \Leftrightarrow SiG(OH)_2$	0.4	0.0	s
27.	$SiGH_2 + O^* \Leftrightarrow SiG(OH)H$	0.4	0.0	s
28.	$SiGH + O^* \Leftrightarrow SiG(OH)$	0.4	0.0	s
	(Attachment of H atoms to dangling bonds)			
29.	$SiG(OH)_2 + H \Leftrightarrow SiG(OH)_2H$	1.0	0.0	s
30.	$SiG(OH)H + H \Leftrightarrow SiG(OH)H_2$	1.0	0.0	s
31.	$SiGH_2 + H \Leftrightarrow SiGH_3$	1.0	0.0	s
32.	$SiG(OH) + H \Leftrightarrow SiG(OH)H$	1.0	0.0	s
33.	$SiGH + H \Leftrightarrow SiGH_2$	1.0	0.0	s
34.	$SiG + H \Leftrightarrow SiGH$	1.0	0.0	s
35.	$SiG_3 + H \Leftrightarrow SiG_3H$	1.0	0.0	s
	(Attachment of OH radicals to dangling bonds)			
36.	$SiG(OH)_2 + OH \Leftrightarrow SiG(OH)_3$	1.0	0.0	s
37.	$SiG(OH)H + OH \Leftrightarrow SiG(OH)_2H$	1.0	0.0	s
38.	$SiGH_2 + OH \Leftrightarrow SiG(OH)H_2$	1.0	0.0	s
39.	$SiG(OH) + OH \Leftrightarrow SiG(OH)_2$	1.0	0.0	s
40.	$SiGH + OH \Leftrightarrow SiG(OH)H$	1.0	0.0	s
41.	$SiG + OH \Leftrightarrow SiG(OH)$	1.0	0.0	s
42.	$SiG_3 + OH \Leftrightarrow SiG_3(OH)$	1.0	0.0	s
	(Abstraction of H atoms from saturated species)			
43.	$H + SiG_3H \Leftrightarrow H_2 + SiG_3$	30.3	4000.0	s
44.	$H + SiG(OH)_2H \Leftrightarrow H_2 + SiG(OH)_2$	30.3	4000.0	s
45.	$H + SiG(OH)H_2 \Leftrightarrow H_2 + SiG(OH)H$	30.3	4000.0	s
46.	$H + SiGH_3 \Leftrightarrow H_2 + SiGH_2$	30.3	4000.0	s
47.	$OH + SiG_3H \Leftrightarrow H_2O + SiG_3$	0.14	500.0	s
48.	$OH + SiG(OH)_2H \Leftrightarrow H_2O + SiG(OH)_2$	0.14	500.0	s
49.	$OH + SiG(OH)H_2 \Leftrightarrow H_2O + SiG(OH)H$	0.14	500.0	s
50.	$OH + SiGH_3 \Leftrightarrow H_2O + SiGH_2$	0.14	500.0	s
	(Dissociative attachment of H_2O to doubly unsaturated species)			
51.	$H_2O + SiG(OH) \Leftrightarrow SiG(OH)_2H$	120.0	5000.0	s
52.	$H_2O + SiGH \Leftrightarrow SiG(OH)H_2$	120.0	5000.0	s
53.	$H_2O + SiG \Leftrightarrow SiG(OH)H$	120.0	5000.0	s
	(Dissociative attachment of H_2O_2 to doubly unsaturated species)			
54.	$H_2O_2 + SiG(OH) \Leftrightarrow SiG(OH)_3$	0.1	0.0	s
55.	$H_2O_2 + SiGH \Leftrightarrow SiG(OH)_2H$	0.1	0.0	s
56.	$H_2O_2 + SiG \Leftrightarrow SiG(OH)_2$	0.1	0.0	s

	Reaction	A	C	Notes
	(Dissociative attachment of H_2 to doubly unsaturated species)			
57.	$H_2 + SiG(OH) \Leftrightarrow SiG(OH)H_2$	0.417	1000.0	s
58.	$H_2 + SiGH \Leftrightarrow SiGH_3$	0.417	1000.0	s
59.	$H_2 + SiG \Leftrightarrow SiGH_2$	0.417	1000.0	s
	(Saturation of surface by HO_2)			
60.	$HO_2 + SiG(OH)_2 \Rightarrow O_2 + SiG(OH)_2H$	0.1	0.0	s
61.	$HO_2 + SiG(OH)H \Rightarrow O_2 + SiG(OH)H_2$	0.1	0.0	s
62.	$HO_2 + SiGH_2 \Rightarrow O_2 + SiGH_3$	0.1	0.0	s
63.	$HO_2 + SiG(OH) \Rightarrow O_2 + SiG(OH)H$	0.1	0.0	s
64.	$HO_2 + SiGH \Rightarrow O_2 + SiGH_2$	0.1	0.0	s
65.	$HO_2 + SiG \Rightarrow O_2 + SiGH$	0.1	0.0	s
66.	$HO_2 + SiG_3 \Rightarrow O_2 + SiG_3H$	0.1	0.0	s
	(Quenching of metastable species)			
67.	$Ar^* \Rightarrow Ar$	1.0	0.0	s
68.	$O^* \Rightarrow O$	1.0	0.0	s
	(Ion-assisted intramolecular elimination of H_2 and H_2O)			
	(Yield parameters: A= 0.2, E_{th}= 0.00, b= 0.5, c= 1.0)			
69.	$X^+ + E + ySiG(OH)_3 \Rightarrow X + ySiG_3(OH) + yH_2O$	1.0	0.0	b, ‡
70.	$X^+ + E + ySiG(OH)_2H \Rightarrow X + ySiG_3(OH) + yH_2$	1.0	0.0	b, ‡
71.	$X^+ + E + ySiG(OH)H_2 \Rightarrow X + ySiG_3H + yH_2$	1.0	0.0	b, ‡
	(Ion recombination on non-reacting surface sites)			
72.	$X^+ + E + SiG_3H \Rightarrow X + SiG_3H$	1.0	0.0	b, *
73.	$X^+ + E + SiGH_3 \Rightarrow X + SiGH_3$	1.0	0.0	b, *
74.	$X^+ + E + SiG(OH)_2 \Rightarrow X + SiG(OH)_2$	1.0	0.0	b, ‡
75.	$X^+ + E + SiG(OH)H \Rightarrow X + SiG(OH)H$	1.0	0.0	b, ‡
76.	$X^+ + E + SiGH_2 \Rightarrow X + SiGH_2$	1.0	0.0	b, ‡
77.	$X^+ + E + SiG(OH) \Rightarrow X + SiG(OH)$	1.0	0.0	b, ‡
78.	$X^+ + E + SiGH \Rightarrow X + SiGH$	1.0	0.0	b, ‡
79.	$X^+ + E + SiG \Rightarrow X + SiG$	1.0	0.0	b, ‡
80.	$X^+ + E + SiG_3 \Rightarrow X + SiG_3$	1.0	0.0	b, ‡
81.	$X^+ + E + SiG_3(OH) \Rightarrow X + SiG_3(OH)$	1.0	0.0	b, †

[b] The reaction-rate parameters are reaction probabilities for Bohm fluxes.

‡ Here X^+ represents all positive ions (Ar^+, O_2^+, O^+, SiH_3^+, SiH_2^+, SiH^+, Si^+, H_2^+, and H^+), while X represents the corresponding neutral species (Ar, O_2, O, SiH_3, SiH_2, SiH, Si, H_2, and H, respectively), where these ions are treated equivalently for the specified reaction path.

* Here X^+ represents all positive ions except O^+ (Ar^+, O_2^+, SiH_3^+, SiH_2^+, SiH^+, Si^+, H_2^+, and H^+), while X represents the corresponding neutral species (Ar, O_2, SiH_3, SiH_2, SiH, Si, H_2, and H, respectively), where these ions are treated equivalently for the specified reaction path.

	Reaction	*A*	*C*	Notes
	(Ion incorporation into the bulk)			
82.	$SiH_3^+ + E + SiG_3(OH) \Rightarrow SiO_2(D) + SiGH_2 + H_2$	1.0	0.0	b
83.	$SiH_2^+ + E + SiG_3(OH) \Rightarrow SiO_2(D) + SiGH + H_2$	1.0	0.0	b
84.	$SiH^+ + E + SiG_3(OH) \Rightarrow SiG + SiO_2(D) + H_2$	1.0	0.0	b
85.	$Si^+ + E + SiG_3(OH) \Rightarrow SiO_2(D) + SiGH$	1.0	0.0	b
86.	$O^+ + E + SiG_3H \Rightarrow SiG_3(OH)$	1.0	0.0	b
87.	$O^+ + E + SiGH_3 \Rightarrow SiG(OH)H_2$	1.0	0.0	b
	(Physical sputtering of SiO_2 by ions)			
88.	$Ar^+ + E + ySiO_2(D) \Rightarrow ySiO_2 + Ar$	1.0	0.0	b
	Yield parameters: A= 2.305E-02, E_{th}= 35 eV, b= 0.5, c= 1.0			
89.	$O^+ + E + ySiO_2(D) \Rightarrow ySiO_2 + O$	1.0	0.0	b
	Yield parameters: A= 1.153E-02, E_{th}= 35 eV, b= 0.5, c= 1.0			
90.	$O_2^+ + E + ySiO_2(D) \Rightarrow ySiO_2 + O_2$	1.0	0.0	b
	Yield parameters: A= 1.630E-02, E_{th}= 35 eV, b= 0.5, c= 1.0			
91.	$H^+ + E + ySiO_2(D) \Rightarrow ySiO_2 + H$	1.0	0.0	b
	Yield parameters: A= 7.000E-04, E_{th}= 35 eV, b= 0.5, c= 1.0			
92.	$H_2^+ + E + ySiO_2(D) \Rightarrow ySiO_2 + H_2$	1.0	0.0	b
	Yield parameters: A= 1.000E-03, E_{th}= 35 eV, b= 0.5, c= 1.0			
93.	$SiH_3^+ + E + ySiO_2(D) \Rightarrow ySiO_2 + SiH_3$	1.0	0.0	b
	Yield parameters: A= 1.614E-02, E_{th}= 35 eV, b= 0.5, c= 1.0			
94.	$SiH_2^+ + E + ySiO_2(D) \Rightarrow ySiO_2 + SiH_2$	1.0	0.0	b
	Yield parameters: A= 1.614E-02, E_{th}= 35 eV, b= 0.5, c= 1.0			
95.	$SiH^+ + E + ySiO_2(D) \Rightarrow ySiO_2 + SiH$	1.0	0.0	b
	Yield parameters: A= 1.614E-02, E_{th}= 35 eV, b= 0.5, c= 1.0			
96.	$Si^+ + E + ySiO_2(D) \Rightarrow ySiO_2 + Si$	1.0	0.0	b
	Yield parameters: A= 1.614E-02, E_{th}= 35 eV, b= 0.5, c= 1.0			

† Here X^+ represents all positive ions except SiH_x^+ (Ar^+, O_2^+, O^+, H_2^+, and H^+), while X represents the corresponding neutral species (Ar, O_2, O, H_2, and H, respectively), where these ions are treated equivalently for the specified reaction path.

V. MODEL RESULTS AND COMPARISONS TO DATA

We have tested the model described in the previous sections against experimental data measured in three different representative reactors. All of the reactors produce high plasma densities (~10^{11}) at very low pressure (1-20 mTorr). Schematics of the three reactor geometries considered are shown in Figure 2 and are labeled Reactor I, Reactor II, and Reactor III for reference purposes. Reactor I is a laboratory-scale helical resonator that is powered by inductive coils surrounding a quartz tube two inches in diameter.[61] Reactor II is a modification of the Lam Research Corporation TCP reactor that includes multiple ports for probe access. Reactor III represents Lam ECR reactors that include a horn-shaped expansion region between the ECR zone and the substrate location. The effects of magnetic fields and magnet settings are ignored in the model for Reactor III, although they are known to contribute significantly to the plasma uniformity across the wafer surface. Langmuir-probe data in mixtures of argon and oxygen were taken in Reactor II, while actinometry measurements were made in Reactor I. These measurements were made at the University of California at Santa Barbara. Both Langmuir-probe data and deposition-rate measurements were acquired in Reactor III. Langmuir-probe measurements for Reactor III were performed at Lam Research Corporation, while deposition-rate data in Reactor III were measured both at Sandia and at Lam. The details of the experimental measurements will be published elsewhere.[68]

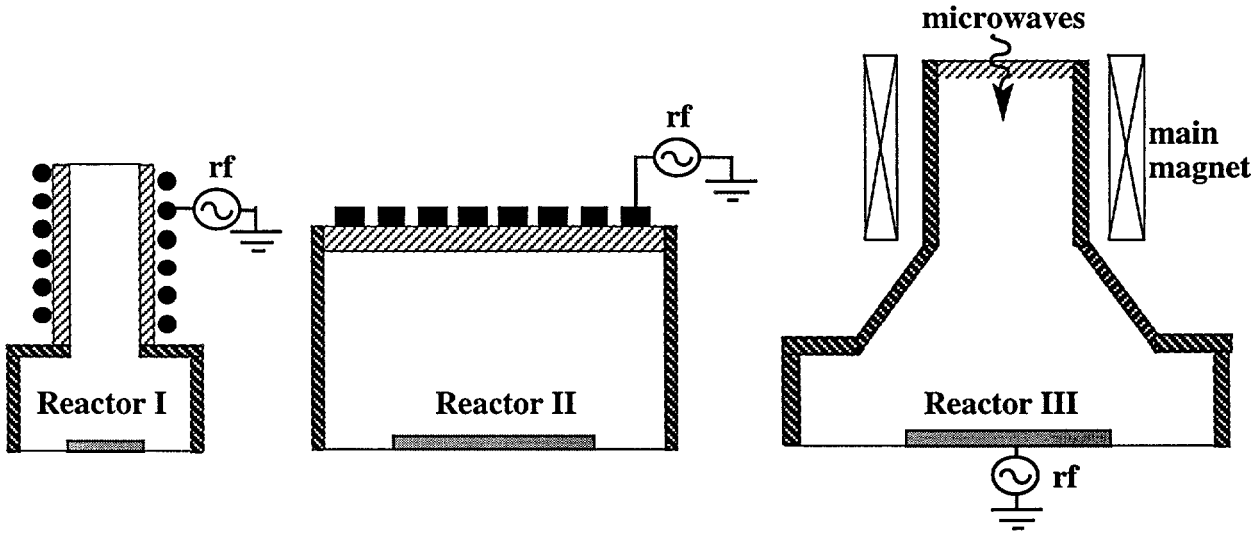

Figure 2. Schematics of three reactors used to collect diagnostic data for model comparisons. Drawings are not to scale and are not intended to provide accurate details of the reactor geometry.

Table III. AURORA Parameters Used in Reactor Simulations

	Reactor I	Reactor II	Reactor III
Reactor Description	Helical Resonator	Transformer-Coupled Plasma	ECR
Reactor Volume (cm^3)	1200.	12000.	12794.
Total Surface Area (cm^2)	800.	3600.	1300.
Deposition Area Fraction	1.0	---	0.32
Main Power (W)	40-250	250-1000	1250-1600
Pressure (mTorr)	5-50	3-15	4.7
Total Flow Rate (sccm)	103.3	50	110-320
ξ for Bohm Fluxes	0.6	0.72	0.6
Ion Energy (eV) (RF bias (W))	15 (0)	15 (0)	85-120 (1260-2400)
Wafer Temperature (K)	300.	330.	553.
Ion Temperature (K)	5800.	5800.	1000.
Heat Transfer Coefficient between reactor and ambient (cal/K-s)	4.7E-4	3.5E-4	4.7E-4

The AURORA model parameters used to capture the behavior of these reactors are shown in Table III. Using a well mixed reactor simulation for plasma modeling requires identification of an effective reactor volume and surface area representative of the activated plasma region. In some cases, the volume is less than the full volume of the reactor due to large expansion areas or plasma confinement. In the parameters listed in Table III, the volume and surface area were calculated based on reasonable approximations of the plasma location and extent; "dead zones" where there is no plasma are not included. For Reactor II, this is the entire volume represented in Fig.2, while in Reactors I and III, the plasma is assumed to fill the upper portions of the reactor and some fraction of the lower region where the wafer resides.

It is also important to note that the total pressure used in the simulations of Reactor III is actually higher than the 2.3-2.7 mTorr measured in the reactor chambers. In the model the total pressure is defined as the sum of all partial pressures, such that:

$$P = \sum_{k=1}^{\#\ species} n_k k_B T_k \tag{6}$$

However, the measurements of electron density and electron temperature in Reactor III indicate that the electron pressure alone is equal to ~2.4 mTorr. For this reason, the pressure used in the model was increased by the measured electron pressure above the measured reactor pressure.

The reactor pressure is measured downstream of the ECR zone and is therefore interpreted as measuring the neutral pressure, rather than the total pressure in the plasma region, as defined by Eq. 6. In Reactors I and II, the electron density is significantly lower than in Reactor III, such that the contribution of electron pressure to total pressure is closer to 10% . In these cases, no correction was made to the measured pressure for use in the simulations.

AR/O_2 ION-DENSITY COMPARISONS TO DATA

Before focusing attention on the complex silicon dioxide deposition chemistry, we begin by discussing model results for argon/oxygen plasmas in reactors II and III. As all of the remaining conditions studied have a large portion of argon and oxygen in the reactor flows, these comparisons build confidence that the well stirred reactor model, using the parameters listed in Table II, can adequately represent the plasma behavior over a sufficiently wide range of operating conditions. Figure 3 shows comparisons of the AURORA model results for argon/oxygen mixtures in Reactor II with total ion density as measured by Langmuir probe. For these experiments there was no rf bias of the substrate. The results show very good agreement over a wide range of power, pressure, and %oxygen. Figure 3(b) shows that the ion density has a very different behavior as a function of pressure when oxygen is present. Based on sensitivity analysis, this appears to be due to an increase in vibrational and electronic excitation processes in oxygen as pressure increases, counteracting the effect of the increase in total density. In Figure 3(a), the conversion of power to increased ion density is less efficient in oxygen, due to the additional dissociation and excitation processes. Dissociative attachment processes also account for a lower production of electrons, although this is not the dominant effect.

In addition to the comparisons with Langmuir-probe data in Reactor II, we have also made comparisons with a limited set of ion-current-density measurements[69] in Reactor III. These results are shown in Figure 4. Here the range of conditions is much smaller than those shown in Figure 3, but the model is still able to capture the subtle trends shown in the measured data. The experimental uncertainty in the probe measurements is on the order of 20%. The comparisons in Figure 4 demonstrate the ability of the AURORA model to capture the behavior of the more complex geometry represented by Reactor III, while keeping the kinetic rate parameters unchanged.

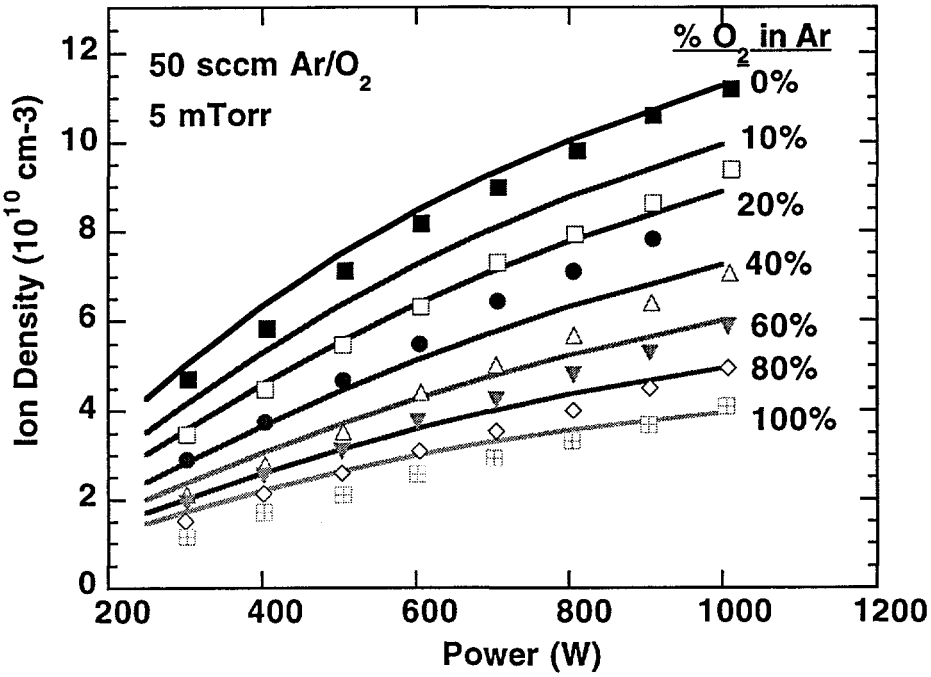

(a)

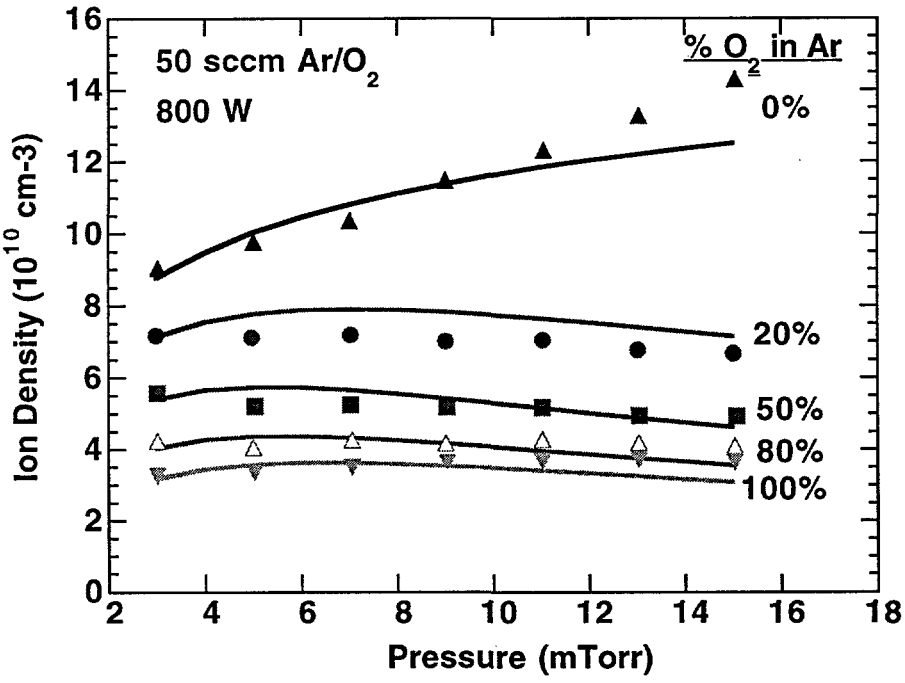

(b)

Figure 3. **Comparison of model predictions of ion density for Ar/O_2 plasmas with Langmuir probe data taken in Reactor II, while varying (a) main power and (b) reactor pressure.**

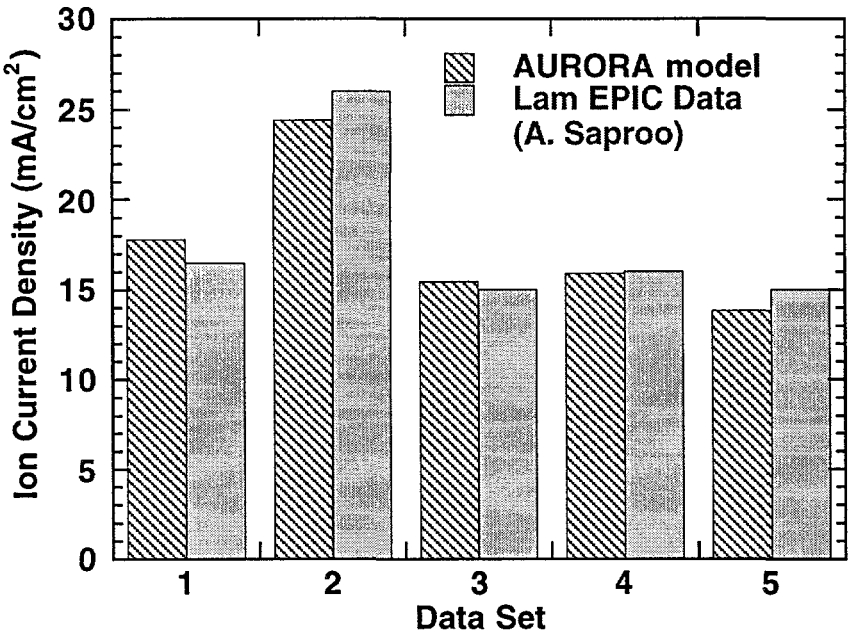

Figure 4. Comparison of model predictions of ion current density with Langmuir-probe data taken in Lam Research Corporation's EPIC reactor,[69] represented by Reactor III. The reactor conditions are not reported here to protect proprietary process recipes.

COMPARISONS WITH ACTINOMETRY DATA FOR O_2/AR/SiH_4 MIXTURES

Upon addition of silane to oxygen/argon mixtures, Langmuir probe measurements become difficult, due to the deposition of oxide material on the probe tip. However, some limited probe experiments have shown little change in the electron density due to the addition of silane. To further our development of the oxygen/argon/silane chemistry system, we compared predictions by the full chemistry model with actinometry measurements made in Reactor I. The details of the actinometry experiments used to obtain relative densities of various species from optical emissions are given elsewhere.[61, 70] We note, however, that the arbitrary units used in Figures. 5-6 are not relative between species. For the actinometry measurements, the gas flow was mainly argon, with 1 sccm SiH_4 and 2.3 sccm O_2. There was no rf bias of the substrate. The ion energy bombarding the surface in the model was therefore assumed to be the plasma potential with a value estimated at 15 eV. Experimentally, the most straightforward measurements are those of O and H atoms, with the interpretation of results more uncertain for SiH and OH radicals. Figures 5 and 6 show comparisons of the model predictions of radical species concentrations as functions of power and pressure with relative measurements of the radical densities by actinometry. As Figs. 5-6 show, the model captures all of the trends observed reasonably well.

In Fig. 5, the increase of power to the helical resonator reactor results in increased O and H radical densities through increased electron-impact dissociation of O_2 and SiH_4, respectively. The SiH radical density actually decreases slightly with increased power primarily due to the neutral gas-phase chemistry between SiH and other radical species. All of the comparisons in Fig. 5 show a discontinuity in plasma behavior at about 40 W power. This discontinuity is also apparent in the experimental data for SiH and OH radical densities, although it is not as pronounced as in the model predictions. We interpret this behavior as an indication of a plasma mode change or a transition to an unstable plasma state at the very low powers. Such transitions are not well simulated by the reactor model employed here.

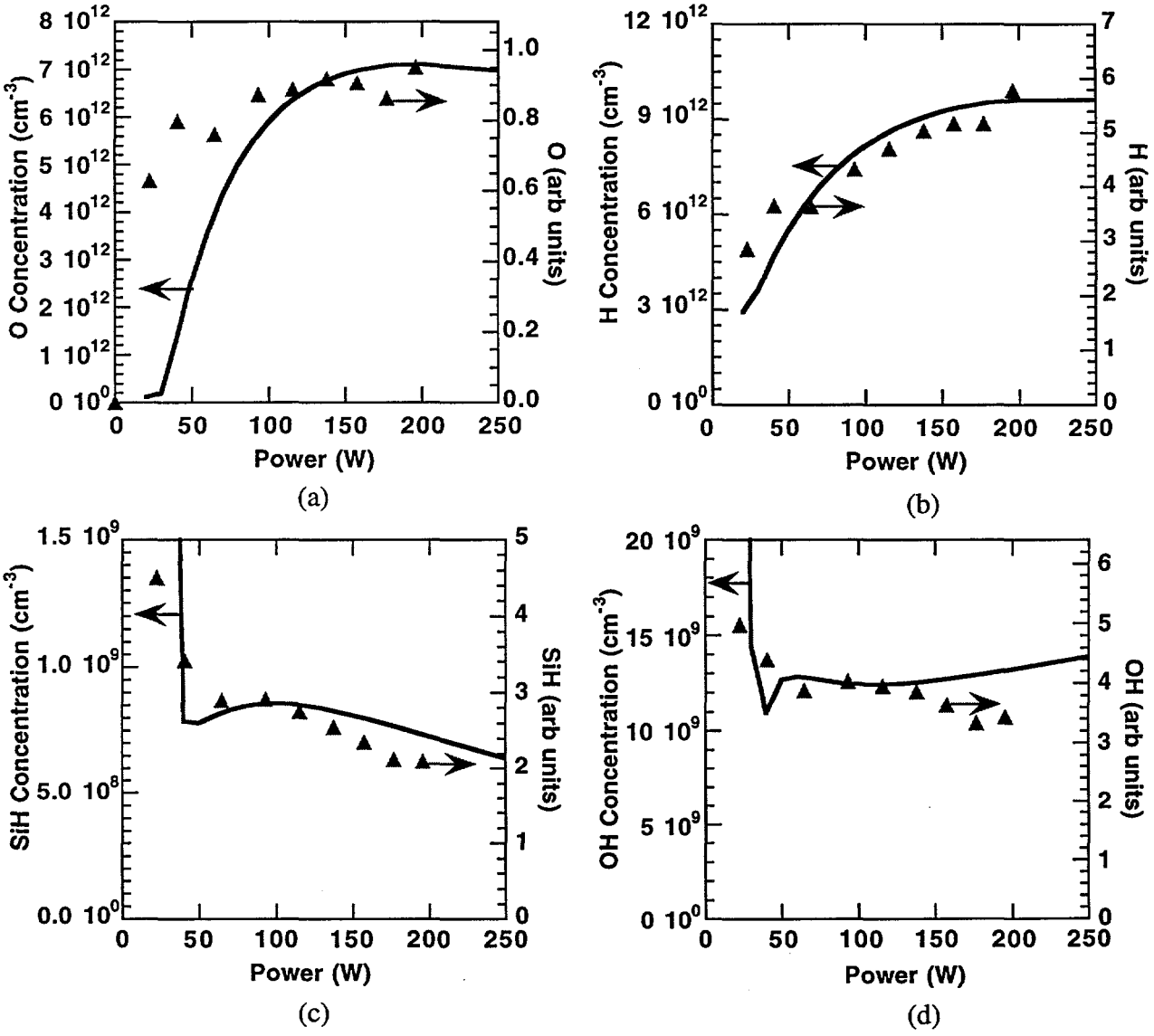

Figure 5. Model predictions of radical densities compared to actinometry measurements for a) O b) H c) SiH and d) OH species as a function of power in Reactor I.

In Fig. 6, the dominant effect on radical densities is the linear increase in total density with pressure. In each of the comparisons, the model is able to predict nearly the same magnitude of change over the pressure range as observed in the actinometry data, in addition to capturing the overall trends. For the OH comparison, the model predicts a slight saturation effect as the pressure increases, which is not observed in the measurements. For our purposes, however, the O, H, and SiH_x radicals play the most important roles in determining deposition behavior, whereas OH interactions with the surface are secondary.

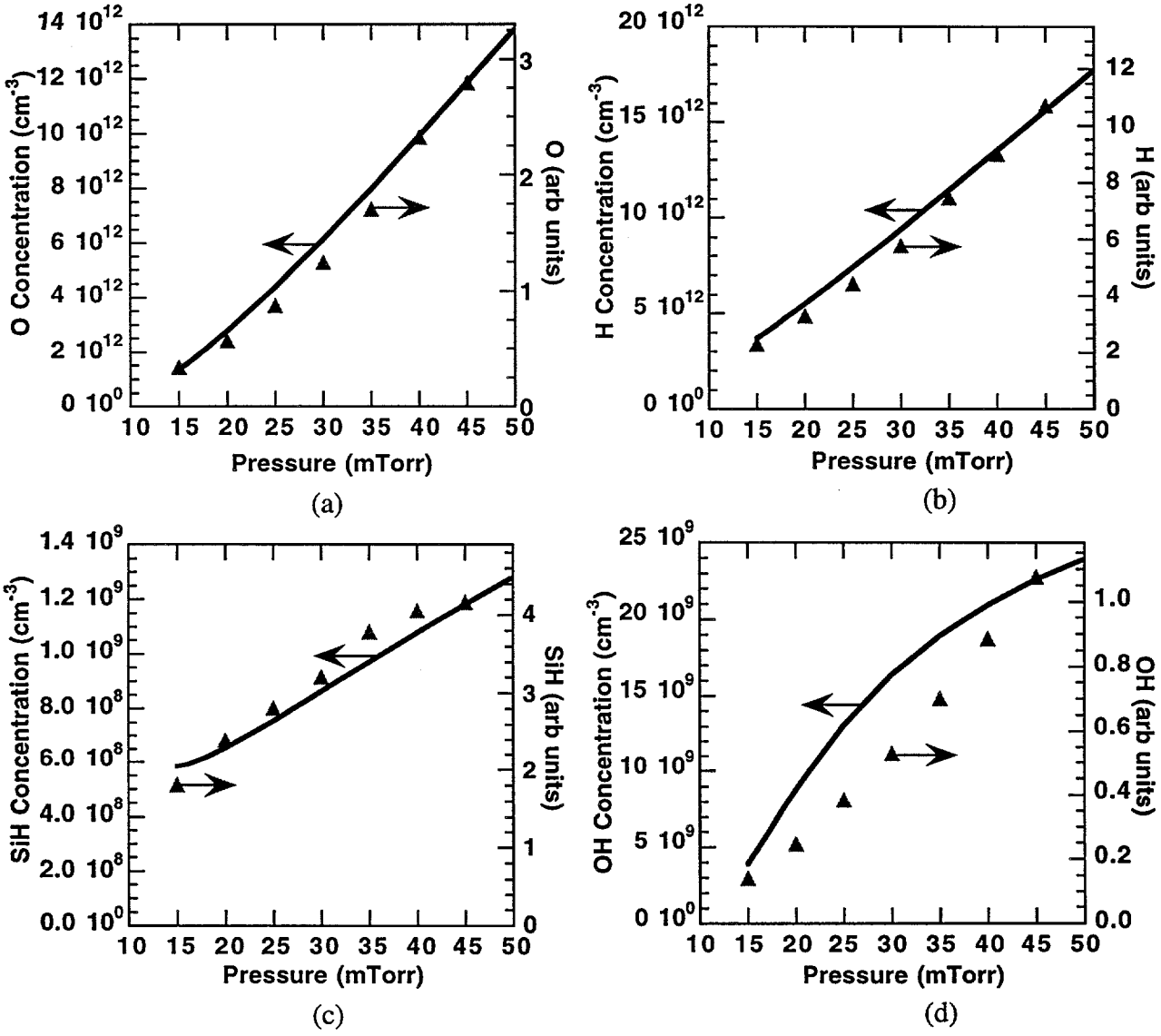

Figure 6. Model predictions of radical densities compared to actinometry measurements for a) O b) H c) SiH and d) OH species as a function of pressure in Reactor I.

COMPARISONS WITH DEPOSITION RATE DATA

Measurements of net oxide deposition rates were obtained in Reactor III. Figure 7 shows the model comparisons with deposition data as a function of the oxygen/silane ratio in the reagent gas mixture. The conditions for these comparisons were 1600 W microwave power, 1260 W rf bias power, 311 sccm total flow rate, and 115-124 sccm of argon. The main magnet current was fixed at 60 A, although this effect is not included in the model. The substrate temperature was maintained at 280 °C. An ion energy of 85 eV was used to capture the effect of the rf bias power, close to the measured dc bias voltage for these conditions. The results in Fig. 7 show quantitative agreement within 10% of the measured deposition rates, which is well within the uncertainty of the experimental.

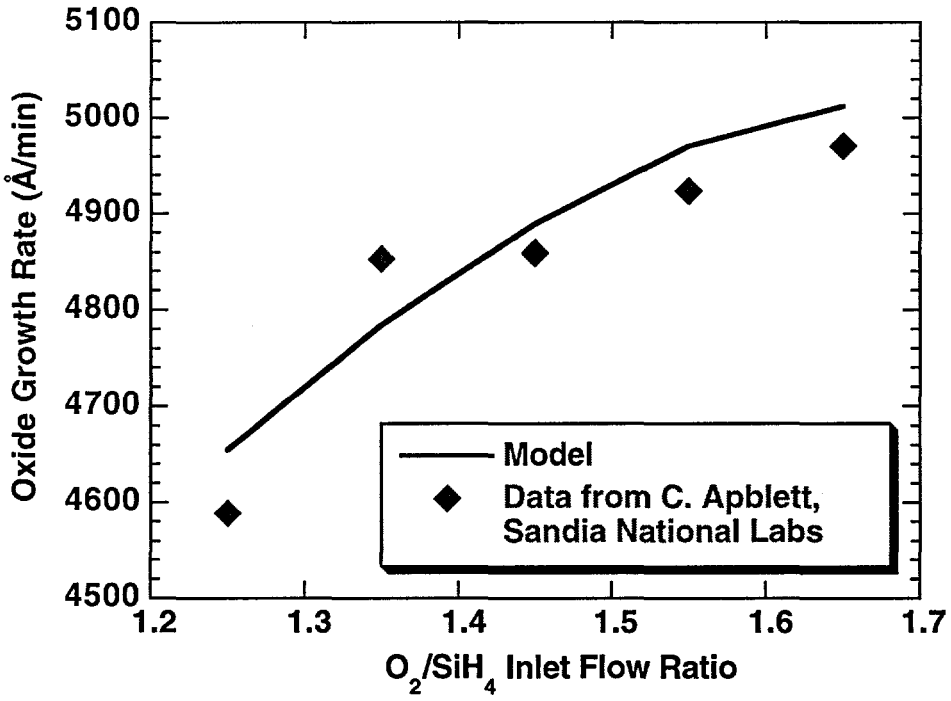

Figure 7. Simulated net deposition rates compared to measurements in a Lam EPIC reactor (Reactor III), as a function of oxygen/silane ratio in the inlet gas.

For the conditions shown in Fig. 7, the net deposition rate is limited by the incorporation of oxygen into the bulk SiO_2. For this reason there is a strong correlation between the deposition rate and the model-predicted oxygen mole fraction in the plasma. At the same time, the SiH_x radical densities decrease as the percent oxygen increases in the inflow. As a result, the net deposition rate displays the opposite trend from the model predictions of the SiH_x and SiO radical densities, despite the fact that these radicals contribute significantly to the net deposition process. Previous experimental work by Chew, et al.,[71] concluded that SiO could not be a precursor to the oxide deposition process based on the fact that the measured SiO density

displayed the opposite trend from measured deposition rates. While conditions in those experiments are significantly different from those described here, our results suggest that their evidence does not appear to be sufficient to rule out SiO as a precursor.

In addition to reagent gas composition, an important parameter in oxide deposition is the substrate temperature. Reproducing deposition trends with substrate temperature is particularly important for the model, as this tests the chemistry model's activation energies as well as the reaction-rate values for a nominal temperature. As shown in Figure 8, the model's prediction of deposition fall-off as a function of wafer temperature agrees well with data from Denison.[72] The conditions in Fig. 8 are 1600 W microwave power, 130 sccm Ar, 113 sccm O_2, 81 sccm SiH_4, 2500 W rf bias power, and a main magnet current of 56 A. For the calculations, we assume an ion energy of 120 eV, consistent with measurements of the dc bias voltage made at Lam.[63] The model is able to capture this behavior due to the inclusion of activation barriers in the surface mechanism and the use of reversible reaction-rate formulations for much of the surface kinetics (that is, for all reactions except those resulting in bulk deposition). As the wafer temperature increases, the rate of radical abstractions and desorption increases, which works against the deposition process and leaves the surface with under-saturated surface species.

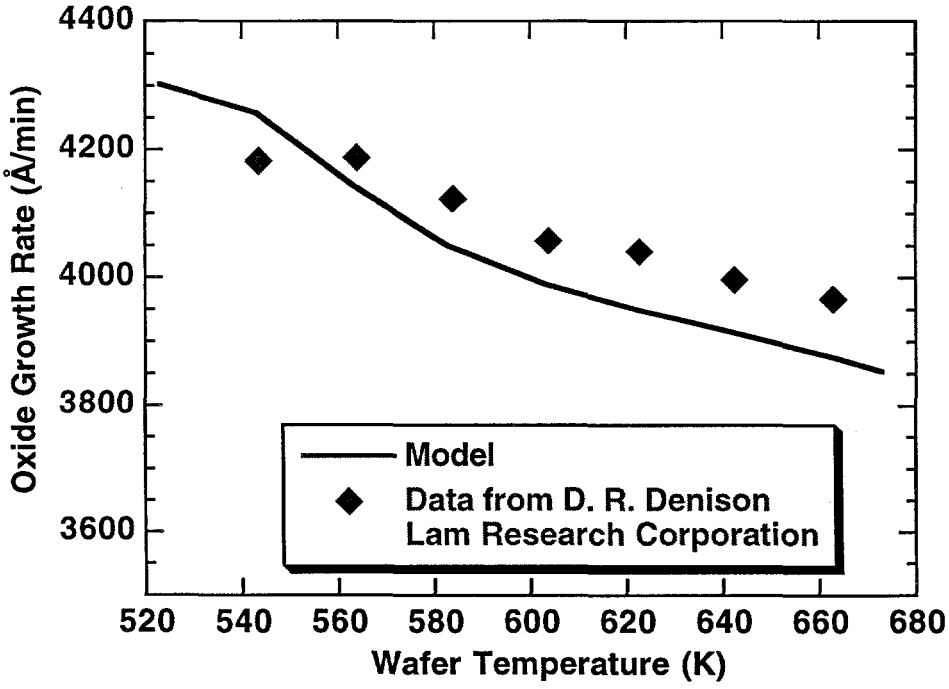

Figure 8. Simulated net deposition rates compared to Denison's[72] measurements in a Lam EPIC reactor (Reactor III), as a function of wafer temperature.

The modeling presented here focuses on the deposition of stoichiometric silicon dioxide. We do not attempt to predict trends that involve changes in morphology or composition of the deposited phase. Neglecting changes in bulk stoichiometry could affect deposition rate comparisons if the model were to be applied well outside of the range of parameters represented by Figures 7-8. The modeling approach taken here is flexible enough to include the effects of bulk composition changes. However, this would require definition of additional surface and bulk phases and further estimates of reaction-rate parameters, and is thus left for future work. Compositional and morphological effects are likely to become increasingly important as circuit-component dimensions shrink and dielectric properties become more critical to the device performance.

DOMINANT REACTION PATHS FOR DEPOSITION SYSTEM

In this section we discuss the dominant reaction paths for a nominal set of reactor conditions and the modifications that were made to the reaction mechanisms in order to obtain the best agreement with the reactor data described in the previous sections. For this purpose the nominal conditions are defined as those of Reactor III running at 1600 W, 4.7 mTorr total pressure, with inlet gas flow rates for O_2, Ar, and SiH_4 equal to 117, 124, and 71 sccm, respectively, and a wafer temperature of 553 K. For this set of conditions, the total net deposition rate predicted by the model was 5140 Å/min. The model also predicts an electron density of 6.2×10^{11}, a mean electron temperature of 4.3 eV, and a gas temperature of 950 K. The molar compositions predicted for the plasma are: 25.5% Ar, 18.5% H, 13.5% H_2, 11.2% O, 9.3% O_2, 6.3% O^*, 4.4% Ar^*, 3.5% SiO, 2.3% SiH, 2.2% SiH_2, 2.0% OH, with less than 2% of each of the remaining species.

The dominant reaction paths are defined as those that contribute most prominently to the determination of the net deposition rate. The importance of the reactions is determined by sensitivity analysis and by examining reaction contributions to net rates of production of species that contribute at least ~5% to the deposition process. The most important gas-phase reactions by this definition are depicted in Fig. 9. Figure 9 shows the paths by which reagent gases are converted to positive ions and radicals that participate in the net deposition process. Although the dominant reactions tend to be electron-impact dissociation and ionization, there are several instances where neutral-radical reactions are also very important. These latter reactions are depicted using double-sided arrows to indicate reversible kinetics. For electron-impact ionization, the paths shown in Fig. 9 are balanced not by gas-phase recombination, but by recombination of ions and electrons at the reactor wall and wafer surfaces, which are not shown in the diagram. Radical species densities also depend on surface reactions, in addition to the reaction paths indicated in Fig. 9.

Figure 10 gives a diagrammatic depiction of the dominant reaction paths from the surface

deposition mechanism listed in Table II. The diagram shows the full cycle of the deposition process. The dominant silicon-containing deposition precursors are SiH and SiH_2, with some contribution from the depositing ions SiH^+, and SiH_2^+. For the nominal conditions, the ion-enhanced elimination of H_2 and H_2O outweighs the corresponding thermal paths. Although not shown in Fig. 10, the ion physical sputtering mechanism (Reactions 88-96 in Table II) is also important in determining the net deposition rate. The dominant ions contributing to both the ion-enhanced elimination and the physical sputtering paths are Ar^+, O^+, SiH^+, and SiH_2^+, as determined by the available ion flux and incident ion momentum.

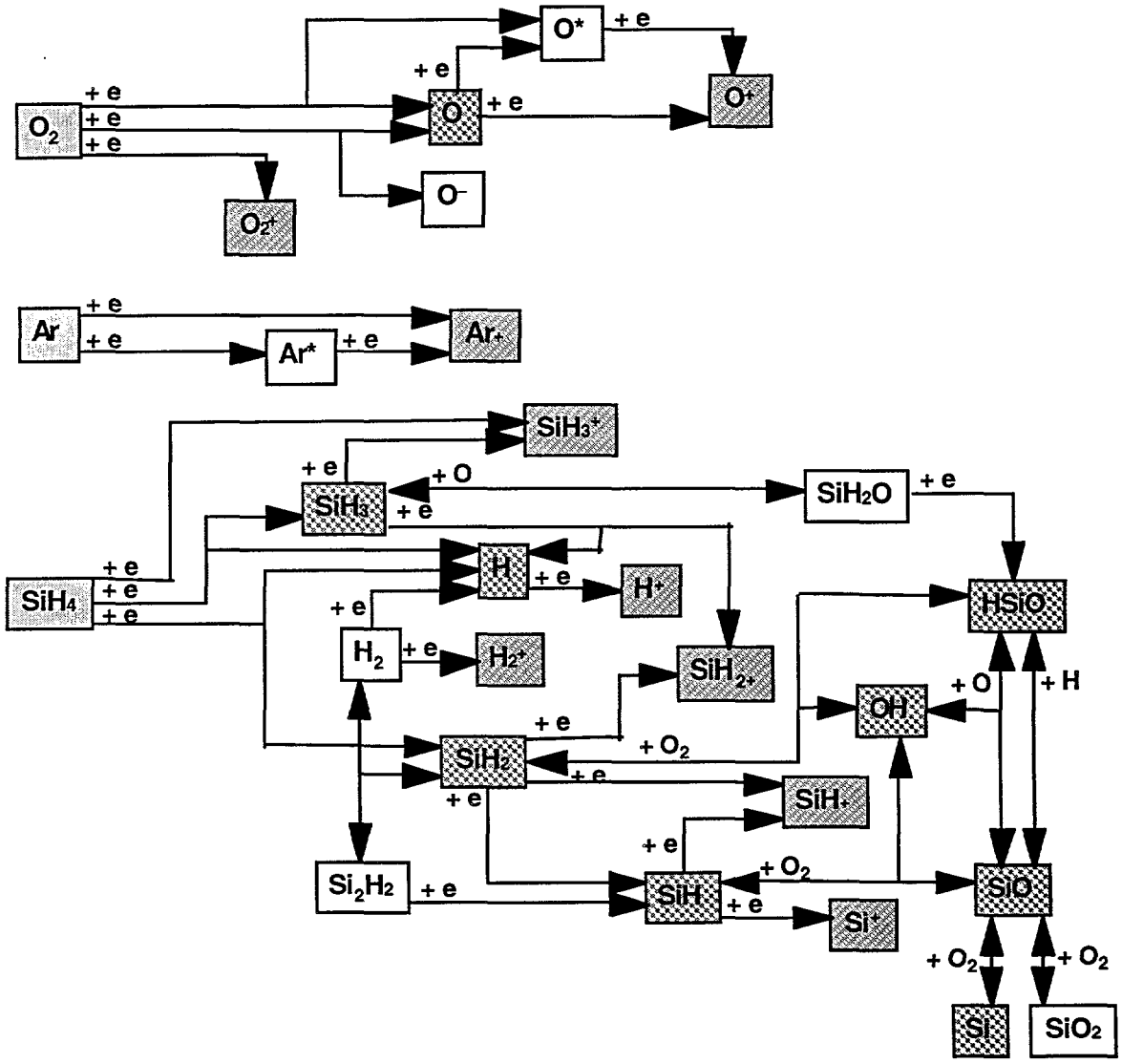

Figure 9. **Schematic showing dominant reaction paths in the plasma gas for nominal conditions. The shaded boxes on the left indicate the reagent gases, while single-cross-hatched boxes indicate ions and the double-cross-hatched boxes indicate radicals that participate in the deposition process.**

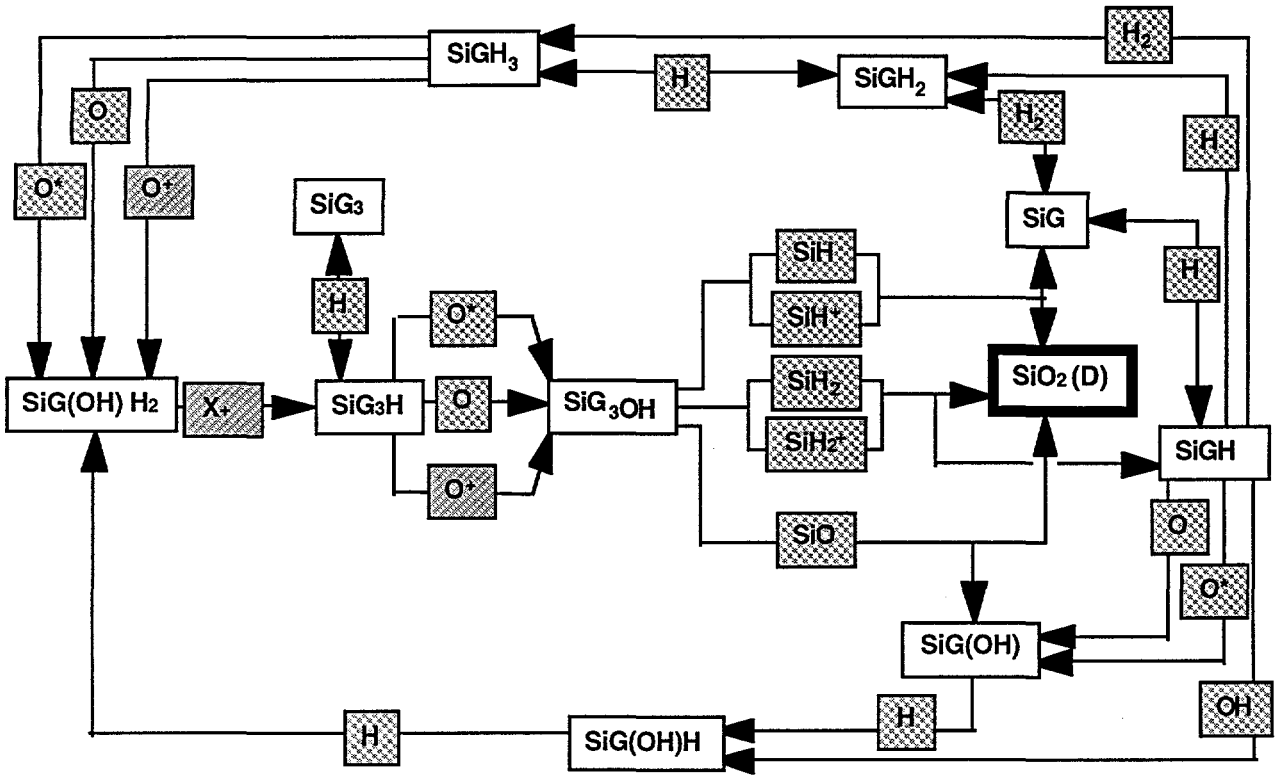

Figure 10. Schematic showing dominant surface reaction paths for nominal conditions. The single-cross-hatched boxes indicate ions and the double-cross-hatched boxes indicate radicals that participate in the deposition process.

As indicated by footnotes on Table I, our final chemical mechanism for the gas-phase reactions involved some modifications to the originally compiled reaction-rate coefficients. First, we added estimates for the electron-impact dissociation of SiH_2O and Si_2H_2, as described in Section III. Second, in making comparisons to the oxide deposition-rate data and the actinometry measurements, we further found it necessary to increase the pre-exponential rate coefficient for Reactions 112 and 122, which control the consumption of oxygen atoms in the gas phase, by a factor of five. This increase, however, is consistent with the observations of Tokuhashi, et al.,[36] who compared their experimental measurements with the silane combustion model that was originally proposed by McLain et al.[73] based on analogies from methane combustion. Tokuhashi, et al. showed that the numerical model was not able to reproduce their experimental results due to an underprediction of the rate of oxidation of SiH_3 using the methane-based rates.[36] The discrepancies were as much as an order of magnitude between the model and experiment. Further modifications were made to Reaction 128, where the pre-exponential rate coefficient was increased by a factor of two, and to Reaction 130, where one half of the published rate coefficient was used. These latter changes result in a net change in the branching ratio of the $SiH_3 + O_2$ reaction by a factor of four, but no significant change in the total reaction rate. We believe that the determination of the branching ratio in the experimental work

by Koshi, et al.,[39] is difficult to quantify and may lead to this degree of uncertainty. In addition, the experiments by Koshi et al. were performed at room temperature, whereas the plasma simulations here predict a gas temperature near 950 K. It is therefore possible that inclusion of activation barriers, if they were known, would lead to a temperature-dependent branching ratio that is consistent both with our findings and those of Koshi et al. In our final adjustment, we removed the activation barrier in Reaction 73 that was originally proposed by Coltrin, et al.[58] Coltrin estimated the reaction-rate coefficients for Reaction 73, but found that this reaction did not actually contribute to the results reported in their work.[74] In fact, the reaction was eventually dropped from their mechanism in a later silane study.[29] As the reaction involves an H abstraction from another radical, it is reasonable to assume a negligible energy barrier. This last adjustment only affected the behavior of the SiH radical density, as compared with actinometry data.

VI. CONCLUSIONS

The model presented here provides a detailed physical picture of the deposition process in HDP reactors depositing silicon dioxide from mixtures of silane, oxygen, and argon. For the gas-phase chemistry we have compiled a set of reactions and reaction rates for the conditions of interest. This reaction mechanism required only minimal adjustment of the published reaction-rate parameters to allow good agreement between model predictions and experimental measurements over a wide range of reactor geometries and operating parameters. Although the description of the surface chemistry is comprised primarily of rough estimates of reaction-rate probabilities, the reaction paths are physically based and sufficiently detailed to allow predictions of complex deposition behavior. The well stirred reactor model, although geometrically simple, is able to reproduce the behavior of the high-density plasmas for three very different reactors. This modeling approach provides computationally fast simulations of complex chemistry systems and can be readily employed in computer-aided design applications. Finally, the comparisons between the model and experimental data highlight the importance of and synergism between modeling and experimental investigations. The complementary efforts allow postulation and testing of reaction paths and dominant mechanisms in realistic reactor environments.

REFERENCES

1 S. E. Lassig, J. Li, J. P. McVittie and C. Apblett, in Proceedings of the DUMIC Conference, ISMIC, p. (1995).

2 J. Li, PhD thesis, Stanford University, 1996.

3 J. Li, J. P. McVittie, J. Ferziger, K. C. Saraswat and J. Dong, Journal of Vacuum Science and Technology B, **13**, 1867 (1995).

4 E. Meeks and J. W. Shon, IEEE Transactions on Plasma Science, **23**, 539 (1995).

5 E. Meeks, H. K. Moffat, J. F. Grcar and R. J. Kee, "AURORA: A Fortran Program for Modeling Well Stirred Plasma and Thermal Reactors with Gas and Surface Reactions," Sandia National Laboratories Report SAND96-8218, 1996.

6 R. J. Kee, F. M. Rupley, E. Meeks and J. A. Miller, "Chemkin-III: A Fortran Chemical Kinetics Package for the Analysis of Gas-Phase Chemical and Plasma Kinetics," Sandia National Laboratories Report SAND96-8216, 1996.

7 R. J. Kee, F. M. Rupley and J. A. Miller, "The Chemkin Thermodynamic Data Base," Sandia National Laboratories Report SAND87-8215B, 1990.

8 M. E. Coltrin, R. J. Kee, F. M. Rupley and E. Meeks, "Surface Chemkin-III: A Fortran Package for Analyzing Heterogeneous Chemical Kinetics at a Solid-Surface - Gas-Phase Interface," Sandia National Laboratories Report SAND96-8217, 1996.

9 C. Lee, D. B. Graves, M. A. Lieberman and D. W. Hess, Journal of the Electrochemical Society, **141**, 1546 (1994).

10 Y. Itikawa, A. Ichimura, K. Onda, K. Sakimoto, K. Takayanagi, Y. Hatano, M. Hayashi, H. Nishimura and S. Tsurubuchi, Journal of Physical and Chemical Reference Data, **18**, 23 (1989).

11 Y. Itikawa and A. Ichimura, Journal of Physical and Chemical Reference Data, **19**, 637 (1990).

12 P. Cosby, Journal of Chemical Physics, **98**, 9560 (1993).

[13] M. Kurachi and Y. Nakamura, IEEE Transactions on Plasma Science, **19**, 262 (1991).

[14] R. Nagpal and A. Garscadden, Journal of Applied Physics, **75**, 703 (1994).

[15] E. Krishnakumar and S. K. Srivastava, Contributions to Plasma Physics, **35**, 395 (1995).

[16] G. G. A. Perkins, E. R. Austin and F. W. Lampe, Journal of the American Chemical Society, **101**, 1109 (1979).

[17] A. Gallagher, Journal of Applied Physics, **63**, 2406 (1988).

[18] J. R. Doyle, D. A. Doughty and A. Gallagher, Journal of Applied Physics, **71**, 4771 (1992).

[19] R. K. Janev, W. D. Langer, K. Evans and D. E. Post, *Elementary Processes in Hydrogen-Helium Plasmas* , (Springer-Verlag, New York, 1987).

[20] V. Tarnovsky, H. Deutsch and K. Becker, Journal of Chemical Physics, **105**, 6315 (1996).

[21] J. Perrin, J. P. M. Schmitt, G. D. Rosny, B. Drevillon, J. Huc and A. Lloret, Chemical Physics, **73**, 383 (1982).

[22] S. K. Srivasta, E. Krishnakumar and A. C. d. A. e. Souza, International Journal of Mass Spectrometry and Ion Processes, **107**, 83 (1991).

[23] D. Margreiter, H. Deutsch and T. D. Mark, Contributions to Plasma Physics, **4**, 487 (1990).

[24] M. D. Allendorf and R. J. Kee, Journal of the Electrochemical Society, **138**, 841 (1991).

[25] R. Atkinson and J. N. Pitts, International Journal of Chemical Kinetics, **10**, 1151 (1978).

[26] J. A. Britten, J. Tong and C. K. Westbrook, in Proceedings of the Twenty-Third Symposium (International) on Combustion, The Combustion Institute, Pittsburgh, PA, p. 195, (1990).

[27] L. Ding and P. Marshall, Journal of Chemical Physics, **98**, 8545 (1993).

[28] A. Goumri, W.-J. Yuan, L. Ding, Y. Shi and P. Marshall, Chemical Physics, **177**, 233 (1993).

[29] P. Ho, M. E. Coltrin and W. G. Breiland, Journal of Physical Chemistry, **98**, 10138 (1994).

[30] D. Husain and P. E. Norris, Journal of the Chemical Society, Faraday Transactions 2, **74**, 93 (1978).

[31] J. A. Kerr and S. J. Moss, *CRC Handbook of Bimolecular and Termolecular Gas Reactions* , (CRC Press, Boca Raton, FL, 1981).

[32] J. Mick, M. W. Markus, P. Roth and V. N. Smirnov, Berichte Bunsengesellschaft, Physical Chemistry, **99**, 880 (1995).

[33] H. J. Mick, P. Roth, V. N. Smirnov and I. S. Zaslonko, Kinetics and Catalysis, **35**, 439 (1994).

[34] J. A. Miller and C. F. Melius, Combustion and Flame, **91**, 21 (1992).

[35] M. Nemoto, A. Suzuki, H. Nakamura, K. Shibuya and K. Obi, Chemical Physics Letters, **162**, 467 (1989).

[36] K. Tokuhashi, S. Horiguchi, Y. Urano, M. Iwasaka, H. Ohtani and S. Kondo, Combustion and Flame, **82**, 40 (1990).

[37] V. N. Volintsev, I. S. Zaslonko, V. S. Mikheev and V. N. Smirnov, Kinetics and Catalysis, **27**, 843 (1987).

[38] F. Westley, J. T. Herron and R. J. Cvetanovic, *Compilation of Chemical Kinetic Data for Combustion Chemistry (NSRDS-NBS 73, Parts 1 and 2)* , (U. S. Government Printing Office, Washington, DC, 1987).

[39] M. Koshi, A. Miyoshi and H. Matsui, Journal of Physical Chemistry, **95**, 9869 (1991).

[40] R. E. Olson, J. R. Peterson and J. Moseley, Journal of Chemical Physics, **53**, 3391 (1970).

[41] J. I. Steinfeld, S. M. Adler-Golden and J. W. Gallagher, Journal of Physical and Chemical Reference Data, **16**, 911 (1987).

[42] V. G. Anicich, Journal of Physical and Chemical Reference Data, **22**, 1469 (1993).

[43] B. L. Kickel, J. B. Griffin and P. B. Armentrout, Zeitschrift fur Physik D, **24**, 101 (1992).

[44] A. V. Phelps, Journal of Physical and Chemical Reference Data, **21**, 883 (1992).

[45] J. Perrin, O. Leroy and M. C. Bordage, Contributions to Plasma Physics, **36**, 3 (1996).

[46] M. D. Allendorf, C. F. Melius, P. Ho and M. R. Zachariah, Journal of Physical Chemistry, **99**, 15285 (1995).

[47] M. W. Chase, C. A. Davies, J. R. Downey, D. J. Frurip, R. A. McDonald and A. N. Syverud, Journal Of Physical and Chemical Reference Data, **14, Supplement No. 1**, 1 (1985).

[48] S. E. Stein, NIST Standard Reference Database 25: NIST Structures and Properties. Gaithersburg, MD, U. S. Department of Commerce, (1994).

[49] V. Puech and L. Torchin, Journal of Physics D, **19**, 2309 (1986).

[50] L. R. Peterson and J. E. Allen, Journal of Chemical Physics, **54**, 6068 (1972).

[51] W. R. Thompson, M. B. Shah and H. B. Gilbody, Journal of Physics B, **28**, 1321 (1995).

[52] B. Peart, R. A. Forrest and K. Dolder, Journal of Physics B, **12**, 2735 (1979).

[53] C. Lee, PhD thesis, University of California at Berkeley, 1995.

[54] R. Atkinson, D. L. Baulch, R. A. Cox, R. F. Hampson, J. A. Kerr and J. Troe, Journal of Physical and Chemical Reference Data, **21**, 1125 (1992).

[55] M. Vialle, M. Touzeau, G. Gousset and C. M. Ferreira, Journal of Physics D, **24**, 301 (1991).

[56] T. L. Pollock, H. S. Sandhu, A. Jodhan and O. P. Strausz, Journal of the American Chemical Society, **95**, 1017 (1973).

[57] Y. Matsui, A. Yuuki, N. Morita and K. Tachibana, Japanese Journal of Applied Physics, **26**, 1575 (1987).

[58] M. E. Coltrin, R. J. Kee and G. H. Evans, Journal of the Electrochemical Society, **136**, 819 (1989).

[59] R. G. Gilbert, K. Luther and J. Troe, Ber. Bunsenges. Phys. Chem., **87**, 169 (1983).

[60] H. K. Moffat, TEOS Mechanism Development Notes. (1992).

[61] S. M. Han and E. S. Aydil, Journal of Vacuum Science and Technology A, **14**, 2062 (1996).

[62] M. A. Lieberman and A. J. Lichtenberg, *Principles of Plasma Discharges and Materials Processing* , (John Wiley & Sons, Inc., New York, 1994).

[63] G. Roche and W. R. Harshbarger, Lam Research Corporation, personal communication. (1996).

[64] S. Scaglione, L. Carneve and F. Sarto, Journal of Vacuum Science and Technology A, **12**, 1523 (1994).

[65] V. I. Babushkin, G. M. Matveyev and O. P. Mchedlou-Petrossyan, *Thermodynamics of Silicates* , (Springer-Verlag, New York, 1985).

[66] S. W. Benson, *Thermochemical Kinetics* , (John Wiley and Sons, New York, 1976).

[67] R. Walsh, in *The Chemistry of Organic Silicon Compounds*, S. Patai and Z. Rappoport, Eds. (John Wiley and Sons, London, 1989), p. 371.

[68] E. Meeks, R. S. Larson, P. Ho, S. M. Han, E. Edelberg, E. Aydil and C. Apblett, To be published, (1997).

[69] A. Saproo, Lam Research Corporation, personal communication. (1996).

[70] S. M. Han and E. S. Aydil, Thin Solid Films, **291**, 427 (1996).

[71] K. H. Chew, J. Chen, R. C. Woods and J. L. Shohet, Journal of Vacuum Science and Technology A, **13**, 2483 (1995).

[72] D. R. Denison, in Proceedings of the The 13th International Conference on CVD (Electrochemical Society), The Electrochemical Society, Reno, NV, p. 957 (1995).

[73] A. G. McLain, C. J. Jachimowski and R. C. Rogers, NASA Report Technical Paper 2415, 1985.

[74] M. E. Coltrin, personal communication. (1997).

INITIAL DISTRIBUTION
UNLIMITED RELEASE

Nadeem Alvi
SEMATECH
2706 Montopolis Drive
Austin, TX 78741-6499

Eray Aydil (10)
Department of Chemical & Nuclear Engineering
University of California
Santa Barbara, California 93106-5080

Maria E. Barone
Lam Research Corporation
4650 Cushing Parkway
Fremont, CA 94538-6401

Wenli Z. Collison
Lam Research Corporation
4650 Cushing Parkway
Fremont, CA 94538-6401

Scott Elrod
SEMATECH
2706 Montopolis Drive
Austin, TX 78741-6499

Richard A. Gottscho
Lam Research Corporation
49026 Milmont Drive
Fremont, CA 94538-7394

William R. Harshbarger
Lam Research Corporation
49026 Milmont Drive
Fremont, CA 94538-7394

David Hodul
Lam Research Corporation
49026 Milmont Drive
Fremont, CA 94538-7394

Junling Li
Technology Modeling Associates, Inc.
595 Lawrence Expressway
Sunnyvale, CA 94086-3935

David Rasmussen
SEMATECH
2706 Montopolis Drive
Austin, TX 78741-6499

Juan Rey
Technology Modeling Associates, Inc.
595 Lawrence Expressway
Sunnyvale, CA 94086-3935

Vikram Singh
Lam Research Corporation
4650 Cushing Parkway
Fremont, CA 94538-6470

Michael Shapiro
SEMATECH
2706 Montopolis Drive
Austin, TX 78741-6499

Vahid Vahedi
Lam Research Corporation
4650 Cushing Parkway
Fremont, CA 94538-6470

Walter Worth
SEMATECH
2706 Montopolis Drive
Austin, TX 78741-6499

0367 R. J. Buss, 1812
0601 J. Tsao, 1126
Attn: M. E. Bartram, 1126
W. G. Breiland, 1126
J. R. Creighton, 1126
0601 H. K. Moffat, 1126
0601 M. E. Coltrin, 1126
0601 P. Ho, 1126 (10)
0601 G. H. Hays, 1128
Attn: G. A. Hebner, 1128
P. A. Miller, 1128
M. E. Riley, 1128
0826 W. Hermina, 9111
0827 A. S. Geller, 9114
Attn: T. J. Bartel, 9114
R. B. Campbell, 9114
S. J. Choi, 9114
D. J. Rader, 9114
A. J. Russo, 9114
R. Veerasingam, 9114
0827 M. L. Hudson, 9114
0827 J. Johannes, 9114
0841 P. J. Hommert, 9100
Attn: R. D. Skocypec,9102
J. H. Biffle, 9103
E. D. Gorham, 9104
S. E. Gianoulakis, 9113
A. C. Ratzel, 9112

W. H. Rutledge, 9115
C. W. Peterson, 9116

1077 L. M. Cecchi, 1326
1077 M. G. Blain, 1326
1077 T. L. Meisenheimer, 1326
1077 J. E. Stevens, 1326
1077 R. S. Bennett, 1326
1078 R. S. Blewer, 1305
1078 J. D. McBrayer, 1302
1079 A. D. Romig, 1300
Attn: G. V. Herrera, 1308
P. Esherick, 1311
1084 J. F. Jakubczak, 1323
1084 C. Apblett, 1323 (5)
1111 J. N. Shadid, 9221
1427 P. L. Mattern, 1100
Attn: S. T. Picraux, 1112
J. Nelson, 1113
T. A. Michalske, 1114
G. A. Samara, 1152
E. B. Stechel, 1153
9001 T. Hunter, 8000
Attn: J. B. Wright, 2200
A. West, 8200
R. C. Wayne, 8400
P. N. Smith, 8500
L. A. Hiles, 8800
9042 C. M. Hartwig, 8345
9042 G. H. Evans, 8345
9042 J. F. Grcar, 8345
9042 S. K. Griffiths, 8345
9042 W. G. Houf, 8345
9042 R. S. Larson, 8345 (10)
9042 A. E. Lutz, 8345
9042 E. Meeks, 8345 (30)
9042 C. D. Moen, 8345
9042 R. H. Nilson, 8345
9042 F. M. Rupley, 8345
9042 P. A. Spence, 8345
9042 A. Ting, 8345
9042 W. S. Winters, 8345
9052 M. D. Allendorf, 8361
9053 R. W. Carling, 8362
9053 S. R. Vosen, 8362
9054 W. J. McLean
Attn: C. W. Robinson, 8301
W. Bauer, 8302
J. L. Durant, 8353
R. J. Gallagher, 8366
D. R. Hardesty, 8361
L. A. Rahn, 8351
F. P. Tully, 8353
9162 K. L. Wilson, 8716
9162 R. J. Bastasz, 8716

9162 D. A. Buchenauer, 8716
9214 C. F. Melius, 8117
9403 B. E. Mills, 8713
9403 D. K. Ottesen, 8713
9405 T. M. Dyer, 8700
Attn: M. W. Perra, 8711
M. I. Baskes, 8712
J. C. F. Wang, 8713
G. J. Thomas, 8715
G. A. Benedetti, 8741
M. R. Birnbaum, 8742
P. E. Nielan, 8743
W. A. Kawahara, 8746
D. B. Nelson, 8783
9409 R. H. Stulen, 8250
9409 G. Kubiak, 8250
9021 Technical Communications Department, 8815, for OSTI (10)
9021 Technical Communications Department, 8815/Technical Library, MS 0899, 4414
8099 Technical Library 4414 (4)
9018 Central Technical Files, 8950-2 (3)